ACS APPLIED ELECTRONIC MATERIALS

pubs.acs.org/acsaelm

Article

Enhancement of Blue Doping-Free and Hyperfluorescent Organic Light Emitting Diode Performance through Triplet−Triplet Annihilation in the Derivatives of Anthracene and Carbazole

Oleksandr Bezvikonnyi, Audrius Bucinskas, Pavel Arsenyan,* Alla Petrenko, Zheng-Yu Wei, Jiun-Haw Lee, Dmytro Volyniuk, Ehsan Ullah Rashid, Tien-Lung Chiu,* and Juozas Vidas Grazulevicius*

Cite This: *ACS Appl. Electron. Mater.* 2024, 6, 4489−4503

Read Online

ACCESS | Metrics & More | Article Recommendations | Supporting Information

ABSTRACT: Carbazoles with *tert*-butyl, methoxy, and methoxyethoxy groups are linked with anthracene-based moieties in a series of designed and synthesized compounds with the aim to obtain triplet levels lower than 2 eV and efficient triplet harvesting in electroluminescent devices. The upconversion of triplet excitons is studied theoretically and experimentally. The triplet fusion is responsible for the appearance of blue delayed emission with lifetimes up to 0.15 ms, which is detected for the methoxy-containing compound by photophysical investigation. The *tert*-butylated emitter shows good performance in organic light emitting diodes (OLEDs), reaching an external quantum efficiency of 5.9% with the 1931 Commission Internationale de l'Éclairage coordinates of (0.14, 0.12). The time-of-flight measurements demonstrate that the derivative of *tert*-butylcarbazolyl and anthracene is the most promising candidate for electronic devices due to its high hole mobility, reaching 7.6×10^{-5} cm^2/(V s) at an electric field of 8×10^5 V/cm. Exploitation of a guest−host containing the *tert*-butylcarbazolyl and anthracene derivative as a host exhibiting triplet−triplet annihilation (TTA) and a fluorescent emitter resulted in an efficient hyperfluorescent OLED with a maximum external quantum efficiency of 7.1%. The OLED with such efficiency outperformed the theoretical limit of conventional fluorescence-based devices due to the utilization of triplet excitons in emission allocated to TTA upconverted excitons.

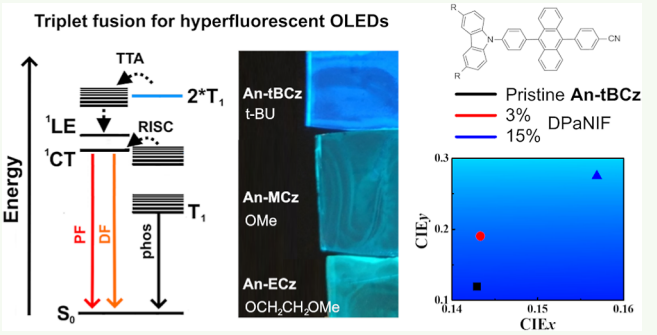

KEYWORDS: *triplet−triplet annihilation, OLED, hyperfluorescence, anthracene, carbazole*

INTRODUCTION

The technology of organic light emitting diodes (OLEDs) needs to solve the issue of the stability and efficiency of devices, especially those with the blue color of emission, for the further advancement in the market of displays and lighting devices.[1−3] Nowadays, OLED displays and lighting devices waste ca. 50% of their power because of the low efficiency of the blue fluorescent emitters currently used in OLEDs.[4,5] In addition, blue pixels often account for ca. 50% of the total display structure, along with red and green pixels.[6] Extrinsic factors such as encapsulation of the OLEDs, upgraded substrates, and so forth can affect the device fabrication and its operational work. They are exploited in trying to improve the stability of the diodes including those emitting blue light.[1] On the other hand, the improvement of the characteristics of organic semiconductors used in OLEDs is an important activity that may allow the improvement of the stability and efficiency of OLEDs.

When electricity is applied, singlet and triplet excitons are formed in the ratio of 1 to 3 in OLEDs due to spin statistics.[1,7] The utilization of triplet excitons in electroluminescence (EL) is considered for the increase in efficiency of the diodes. Several approaches have been introduced aiming to stimulate triplet exciton emission. They include phosphorescence of noble metal complexes, thermally activated delayed fluorescence (TADF), room-temperature phosphorescence (RTP) of organic emitters, and reverse intersystem crossing (RISC) via hybridized local charge transfer (HLCT) states.[1,8−12] Although significant improvements have been made in the design and application of emitters exhibiting the above-mentioned phenomena, they all have their own limitations and require further modification. The limitations are related to the operational stability, color quality, energy consumption, cost

Received: March 27, 2024
Revised: May 30, 2024
Accepted: May 31, 2024
Published: June 12, 2024

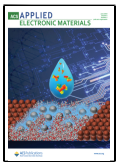

efficiency, and environmental pollution.[1] Blue phosphorescent and TADF emitters developed to date are not stable enough for industrial use.[13] The high-energy and long lifetime of excited triplet states of phosphorescent and TADF emitters are the main reasons for the limited stability of blue organic electroluminescent devices.[14,15] Different strategies were exploited to overcome the limitations of TADF and phosphorescent emitters. For example, the control of the host morphology for boosting the stability and efficiency of deep-blue PhOLEDs and phosphor-sensitized TADF emission systems were developed.[16,17] The deep-blue emitting devices with the external quantum efficiency of ca. 22−26% and operational lifetime significantly longer than that of the conventional deep-blue devices were obtained.[16,17] However, the use of noble metals for such emissive complexes remains problematic from the environmental point of view.[1]

Fortunately, it is possible to achieve the η_{EQE} higher than the theoretical limit of 5% of OLEDs with the conventional fluorescent emitters.[18] This can be done by exploiting low-energy excited triplet states, e.g., through triplet−triplet annihilation (TTA). TTA is a nonlinear process, i.e., yielding nonlinear increments in excitation in this case, of utilization of the triplet electronic excitation energy.[19,20] This is considered to be one of the primary reasons for the efficiency roll-off of OLEDs.[21] However, TTA itself can be used as a tool for increasing the efficiency of the triplet emitters by upconverting two triplet excitons and generating a singlet exciton of twice higher energy, while the other annihilating species is returned to the ground state.[13] Depending on the alignment of the energy levels of the excited states, the recombination of the exciton can occur directly from this $2{\cdot}T_1$ energy level of a single state or after relaxation to the lower singlet excited state.[22] Triplet fusion provides an opportunity to increase the limit of internal quantum efficiency from 25% for OLEDs based on prompt fluorescent emitters to 62.5% for the devices based on emitters exhibiting TTA. The studies on the TTA contribution to the EQE of the OLEDs remains limited. As TTA was originally studied in detail for pyrene, the historic term for the long-lived emission arising from TTA is p-type delayed fluorescence.[23,24] As the triplet states are involved in creating the exciton, the emission of the newly formed singlet exciton is delayed fluorescence, characterized by long lifetimes, mostly on a microsecond scale. The lifetimes are considerably longer than those of the original excitons deactivated through prompt fluorescence. The diffusion control model of the sensitizer−annihilator system or the so-called producer−promoter system is generally considered for TTA systems.[13,25] According to this model, a molecule of the sensitizer is photoexcited, populating triplet excited states through intersystem crossing (ISC) from singlet excited states. Subsequently, hopping from the sensitizer to a molecule of the annihilator occurs through triplet−triplet energy transfer (TTET) by the Dexter exchange mechanism, populating the triplet excited states of the annihilator.[13,25] TTA is initiated in the intermolecular interaction of two annihilator molecules once a sufficient population of the annihilators is reached, forcing an encounter between them. Intramolecular TTA in the case of sensitizer−annihilator systems has also been reported.[14] Both TTET and TTA are diffusion-mediated processes relying on the concentrations of the compounds. A single molecule exhibiting delayed fluorescence originated from TTA without approaching the specific intermolecular interactions of two compounds, such as in sensitizer−annihilator systems, is of great demand. It can potentially allow one to simplify the device fabrication by not using a sensitizer. The significant energy losses occur during ISC in a sensitizer and TTET from a sensitizer to an annihilator.[14] Predictably, the shortcomings of TTA-based OLEDs can be addressed by developing new functional materials.

Anthracene-based emitters exhibiting TTA-related delayed fluorescence have attracted great interest over the last years.[26−29] Some of them have a carbazole moiety as a donor.[30,31] They are primarily used as emitters in OLEDs.[32] A relatively new method for efficient harvesting of triplet excitons in OLEDs is based on hyperfluorescence.[33,34] TADF molecules are typically used as cohosts in organic hyperfluorescence systems.[35] The hyperfluorescence approach allows us to achieve higher internal quantum efficiencies (IQEs) and EQEs for OLEDs than those for the devices based on prompt fluorescence.[36] Hyperfluorescence-based systems allow us to reach higher color purity and operational stability for OLEDs than for TADF systems.[37,38] In contrast to conventional TADF-based hyperfluorescence, our investigation partly aimed to explore the applicability of TTA hosts in hyperfluorescent OLEDs.

In this work, we designed and synthesized the derivatives of an anthracene core exhibiting blue TTA emission and studied them as hosts in hyperfluorescent guest−host systems. A large planar conjugated system of anthracene was exploited to ensure molecular packing, stabilizing triplet excitons and inducing intermolecular interactions mediated by carbazole donors. Such interactions resulted in TTA. Molecular packing of anthracene derivatives is known to cause aggregation-caused quenching.[39] The designed structures enable adjustment of the steric hindrance.[40] The carbazole moiety is selected as an electron donor unit because of its known capability of improving thermal stability and charge transport and tuning the energy levels of triplet excited states.[41] The molecular packing in the films of the two compounds from the series is affected by alkoxy groups attached to carbazole moieties. The attachment of alkoxy groups alters the energy levels of molecular orbitals, improving the thermal stability of the compounds and charge balance at recombination sites. These effects manifest due to hydrogen bonding of the oxygen atoms of alkoxy groups and the hydrogen atoms of the interacting molecules.[13] The attachment of the *tert*-butyl group to the carbazole moiety was found to be a pathway for minimization of the loss of energy of triplet excitons via nonradiative deactivation.[42] In this work, the theoretical and experimental analysis of the derivatives of anthracene and carbazole was performed to detect the delayed fluorescence and confirm its TTA origin. The derivative of *tert*-butylcarbazole and anthracene was successfully utilized as both an emitter and a host for blue-emitting OLEDs. Using the new TTA compound, blue TTA-based doping-free and TTA-assisted hyperfluorescent OLEDs were fabricated with maximum EQEs of 5.9 and 7.1%, respectively.

EXPERIMENTAL SECTION

Unless otherwise stated, all reagents were purchased from commercial suppliers and used without further purification. Thin layer chromatography (TLC) was performed using MERCK Silica gel 60 F254 plates and visualized by UV (254 nm) fluorescence. ZEOCHEM silica gel (ZEOprep 60/35−70 μm—SI23501) was used for column chromatography. ^{1}H and ^{13}CNMR spectra were recorded on a Bruker 400 spectrometer at 400 and 101 MHz,

https://doi.org/10.1021/acsaelm.4c00533
ACS Appl. Electron. Mater. 2024, 6, 4489−4503

Scheme 1. Synthesis of Carbazolylphenyl Anthracenylbenzonitriles 7a–c[a]

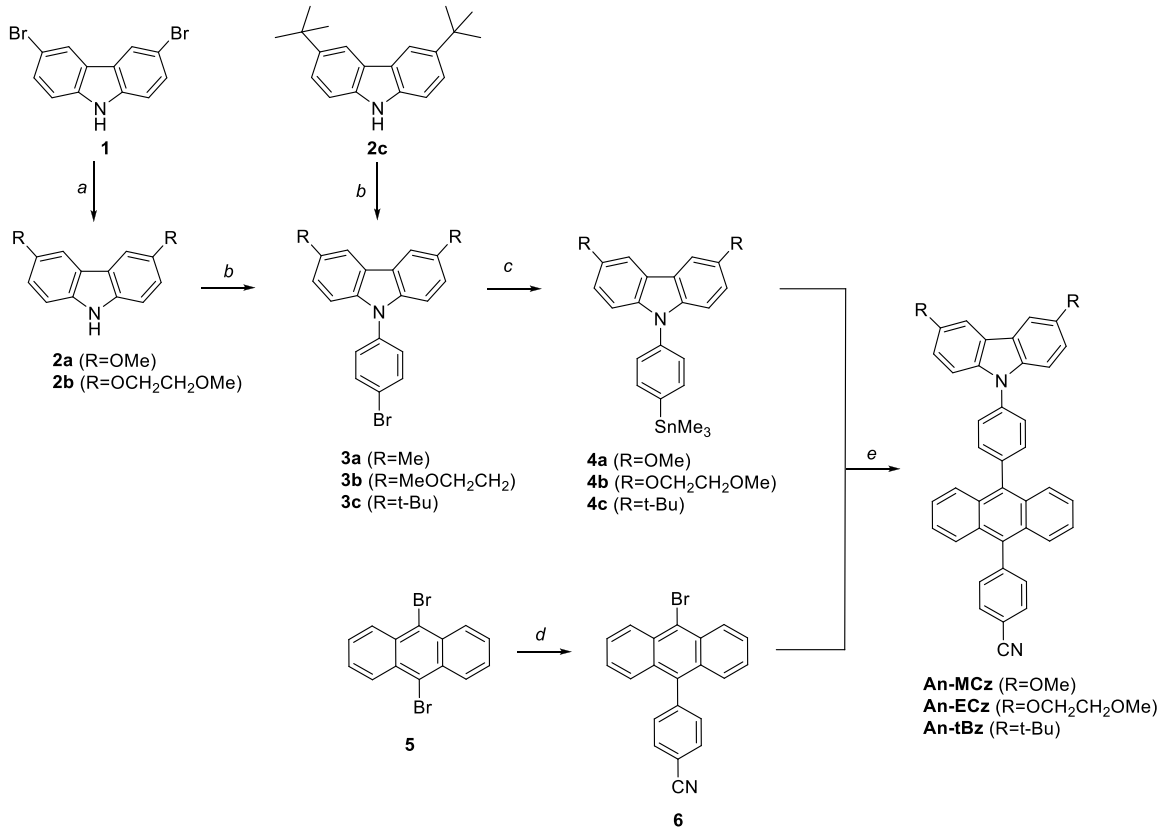

[a]Reaction conditions: (a) excess of sodium methanolate in DMF or sodium methoxyethanolate in methoxyethanol, heating; (b) 4-bromofluorobenzene (1.1 equiv), Cs_2CO_3 (5.0 equiv), NMP, 150 °C, 48 h; (c) *n*-BuLi (1.2 equiv), Me_3SnCl (1.2 equiv), THF, −78 °C; (d) (4-cyanophenyl)boronic acid (1.0 equiv); K_2CO_3 (8.0 equiv), $Pd(PPh_3)_4$ (0.02 equiv), H_2O/toluene/methoxyethanol, 90 °C, 2 h; and (e) **6**, $Pd(PPh_3)_4$ (0.05 equiv), $AsPh_3$ (0.05 equiv), xylene, 120 °C, 12 h.

respectively, at 298 K in $CDCl_3$. The ^1H chemical shifts are given relative to the residual $CHCl_3$ signal (7.26 ppm), ^{13}C—relative to $CDCl_3$ (77.16 ppm). Reagents were purchased from regular vendors, e.g., BLD Pharm, ABCR, TCI Europe, and ACROS.

All density functional theory (DFT)-based computational calculations are done using the Gaussian 16 program,[43] and three-dimensional molecular geometries are drawn and viewed by using GaussView 6. The geometries of An-tCZ, **An-MCz**, and **An-ECz** are optimized at the ground level using the Becke 3-parameters Lee–Yang–Perdew (B3LYP) hybrid functional[44] and 6-31G(d,p) basis set. The impact of the solvent is also computed using the integral equation formalism polarizable continuum model (IEFPCM) for DFT calculations. Reorganization energy (RE) estimations for electron (λ_e) and hole (λ_h) mobilities were also done at B3LYP/6-31G(d,p) for potential analysis of charge transfer properties of compounds. Density of states (DOS) calculations were performed at the B3LYP/6-31G(d,p) level, and plots were generated using PyMOlyze 1.1 software.

Absorption spectra were recorded by an Avantes AvaSpec-2048XL spectrometer. Emission spectra and photoluminescence (PL) quantum yields (Φ) were determined using an Edinburgh Instruments' FLS980 fluorescence spectrometer. Φ was estimated using an integral sphere by an absolute method. PL decay curves and transient PL spectra were measured using FLS980 equipped by the 374 nm laser PicoQuant LDH-D-C-375 and the Edinburgh Instruments uF920H microsecond lamp, for which 350 nm was chosen as the wavelength of photoexcitation. A Pfeiffer HiCUBE pump and an Optistat DN2 cryostat were utilized for the measurement at deoxygenated conditions and low temperatures.

We utilized the highly reliable time-of-flight (TOF) method to precisely characterize charge transport in organic materials **An-tBCz**, **An-MCz**, and **An-ECz** for accurate determination of hole and electron mobilities in vacuum-deposited layers of the investigated compounds. A more than 1 μm thick organic layer of **An-tBCz**, **An-MCz**, and **An-ECz** as the active medium, indium–tin oxide (ITO) as the bottom electrode, and aluminum as the top electrode were used in our TOF experiments. The layers were kept pure and intact by carrying out the deposition process under a vacuum of 2×10^{-6} mbar. In our experimental setup, we utilized an EKSPLA laser with a wavelength of 355 nm as the excitation source to generate charge carriers within the organic layer. By applying various positive and negative external voltages to the samples using the Keithley precision 6517B electrometer, we investigated the hole and electron transport under different electric fields. We used the TDS 3032C oscilloscope made by Tektronix to measure the transit time (t_{tr}) of charge carriers. By recording the photocurrent transients of either holes or electrons for layers of **An-tBCz**, **An-MCz**, and **An-ECz**, we were able to estimate the charge mobilities (μ) using the formula $\mu = d^2/(V \times t_{tr})$, where d represents the thickness of the organic layer and V corresponds to the applied voltage over the sample. Thicknesses (d) of organic layers of **An-tBCz**, **An-MCz**, and **An-ECz** were determined by the profilometer Profilm3D (Figure S11).

The process of the bottom-emission OLED fabrication used an indium tin oxide (ITO) substrate to be the anode that was treated by oxygen plasma to clean its surface and also increase its work function (from 4.9 to 5.1 eV) to reduce the energy barrier at the anode/organic layer interface. The organic layers and inorganic cathode were deposited by using a multisource evaporator with an ultrahigh vacuum. For device encapsulation, all devices were encapsulated with a transparent cover glass and sealed with ultraviolet glue inside a glovebox (N_2 ~99.95%). The electrical and optical characteristics of devices were measured by a L–J–V system consisting of a

https://doi.org/10.1021/acsaelm.4c00533
ACS Appl. Electron. Mater. 2024, 6, 4489–4503

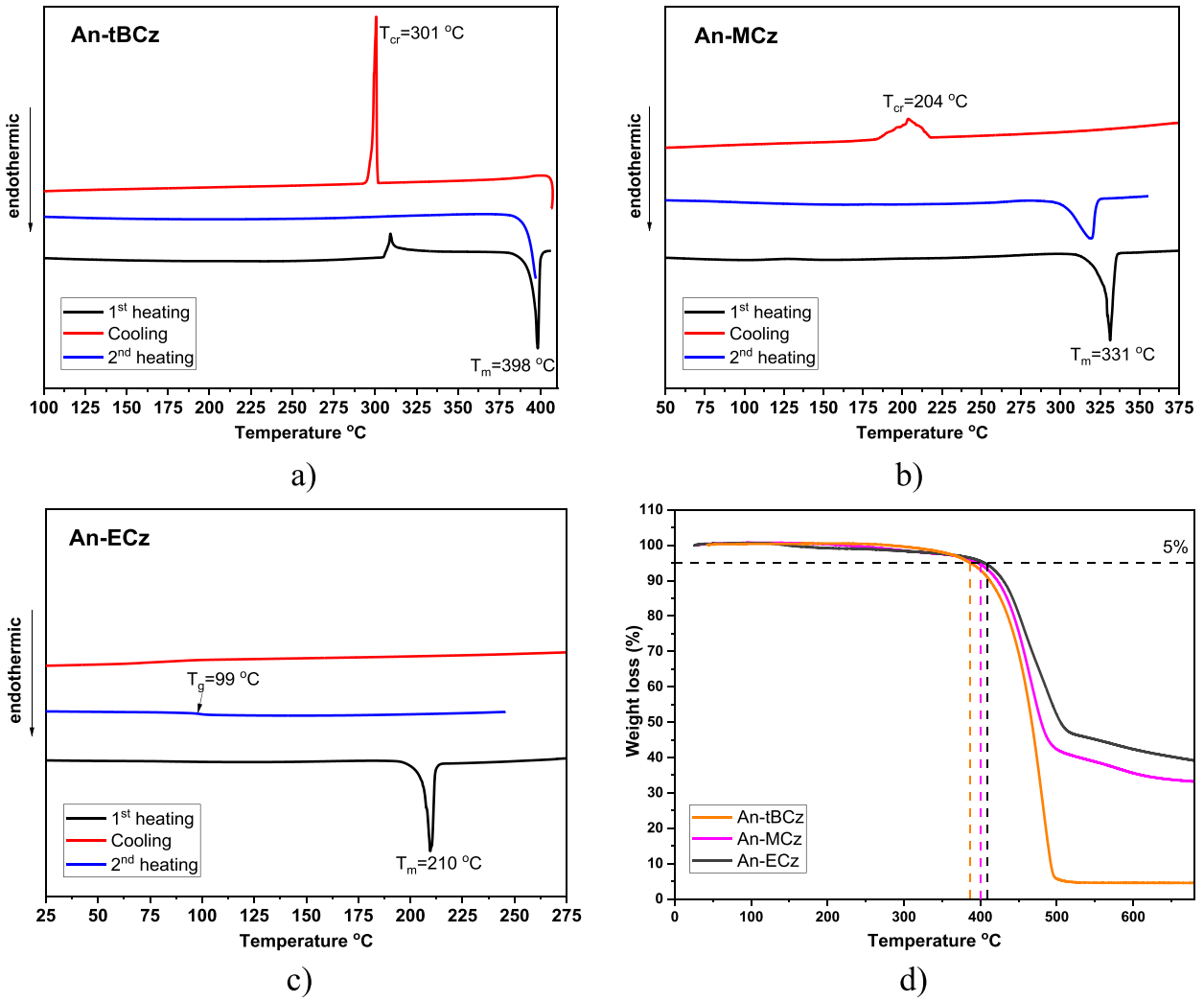

Figure 1. DSC curves of **An-tBCz** (a), **An-MCz** (b), and **An-ECz** (c) and TGA curves of the compounds (d) recorded in a nitrogen atmosphere and the scan rate of 20 °C/min.

multisource meter (Keithley 2400) and a spectrometer (Minolta CS1000), such as current density versus driving voltage ($J-V$), luminance versus driving voltage ($L-V$), emission spectrum, color coordinates, current efficiency (η_{CE}), power efficiency (η_{PE}), external quantum efficiency (η_{EQE}), and operational lifetime. The further carrier and exciton dynamics were analyzed by using a transient electroluminescence (TrEL) system, whose setup consisted of a waveform function generator (Agilent 335011B) to drive the OLED and a photomultiplier (Hamamatsu, H6780-20) as well as an oscilloscope (Tektronix, TSB2202B) to collect and record the optical signal form the OLED. Some of the $L-J$ dependences for the evaluation of slopes were recorded using a calibrated PH100-Si-HA-D0 photodiode, a Keithley 2400C SourceMeter, a 11S-LINK Power and Energy Monitor, and a 6517B electrometer.

RESULTS AND DISCUSSION

Synthesis. The preparation of the desired carbazolyl phenyl anthracenyl benzonitriles and **An-MCz**, **An-ECz**, and **An-tBCz** was started with the treatment of 3,6-dibromocarbazole (**1**) with sodium methanolate and methoxyethanolate, yielding the corresponding 3,6-dimethoxycarbazole (**2a**) and 3,6-bis(2-methoxyethoxy)-9*H*-carbazole (**2b**) in 95 and 97%, respectively (Scheme 1). *N*-Bromophenylcarbazoles **3a−c** were obtained from the reaction of **2a−c** with 4-bromofluorobenzene in the presence of an excess of cesium carbonate in *N*-methylpyrollidinone (NMP). We decided to use the Stille coupling protocol for the binding of the carbazolylpenyl moiety to the anthracene fragment as the use of arylboronic acids was not sufficient. Derivatives **3a−c** were converted to the corresponding stannanes **4a−c**. It is important that the derivatives **4a−c** were not purified and used as raw material in the next step as trimethyltin derivatives are very harmful to human health. 4-(10-Bromoanthracen-9-yl)benzonitrile (**6**) was prepared from (4-cyanophenyl)boronic acid and 9,10-dibromoanthracene (**5**) in the presence of potassium carbonate and a catalytic amount of tetrakis-(triphenylphosphine)palladium.[45] It should be noted that the boronic acid must be added in portions; otherwise, the yield is low. As a result, compound **6** was isolated in 61% yield. Finally, the desired products **An-MCz**, **An-ECz**, and **An-tBCz** were obtained by the Stille coupling reaction of **4a−c** with bromoanthracene **6**. The coupling reactions were carried out in the presence of the palladium(0) catalyst $[(Ph_3P)_4Pd]$ and triphenylphosphine as the ligand.[46]

Thermal Properties. Differential scanning calorimetry (DSC) was employed to investigate the thermal transitions such as melting and glass transitions. The DSC curves are shown in Figure 1. The thermal characteristics of the target derivatives (**An-tBCz**, **An-MCz**, and **An-ECz**) are listed in

https://doi.org/10.1021/acsaelm.4c00533
ACS Appl. Electron. Mater. 2024, 6, 4489−4503

Table 1. The DSC traces of the initial heating scans verified the crystalline character of all of the target derivatives. Well-

Table 1. Thermal Characteristics of Compounds An-tBCz, An-MCz, and An-ECz

compound	T_m, (°C)[a] (1st heating s)	T_g, (°C)[b] (2nd heating s)	T_{cr}, (°C)[b] (cooling)	T_d, (°C)[c]
An-tBCz	398		301	387
An-MCz	331		204	399
An-ECz	210	99		407

[a]Melting temperature at the scan rate of 10 °C/min, N_2 atmosphere. [b]Glass transition temperature. [c]5% weight loss temperature at the scan rate of 20 °C/min, N_2 atmosphere.

defined endothermic melting signals at the temperatures ranging from 210 to 398 °C were observed. The highest T_m values were detected for *tert*-butyl- and methoxy-substituted derivatives (**An-tBCz** and **An-MCz**). We presume that the presence of sterically smaller groups can affect the molecular packing of substances, which can lead to higher melting points as more energy is required for the solid-to-liquid transition to overcome the intermolecular forces between molecules. During the DSC cooling scans, notable exothermic crystallization peaks were observed for **An-tBCz** and **An-MCz**. Specifically, **An-tBCz** exhibited a crystallization peak at 301 °C, and **An-MCz** showed a peak at 204 °C. No such crystallization transition was identified for **An-ECz**. Upon analysis of the DSC second heating scans, distinct observations from **An-tBCz** and **An-MCz** were made for **An-ECz**. It presents a stable molecular glass with a transition temperature of 99 °C. In the case of **An-tBCz** and **An-MCz** second heating DSC curves, their crystalline character was reaffirmed with peaks corresponding to the temperatures observed during the first heating scan.

Thermogravimetric analysis (TGA) was used to investigate the thermal stability of the target compounds. The TGA curves of the compounds are shown in Figure 1d. All anthracene derivatives (**An-tBCz**, **An-MCz**, and **An-ECz**) exhibited high thermostability under heat in an inert atmosphere. The 5% weight loss temperature (T_d) ranged from 387 to 407 °C. The derivative enriched with methoxyethoxy groups (**An-ECz**) showed the highest T_d. The elevated T_d values of **An-MCz** and **An-ECz** can also be attributed to the augmented intramolecular forces.

Electrochemical Properties. The electrochemical properties of the DCM solutions of compounds **An-tBCz**, **An-MCz**, and **An-ECz** were assessed by cyclic voltammetry at a 100 mV/s scan rate using ferrocene as an inner standard (Figure 2). The studied compounds having *tert*-butyl (**An-tBCz**), methoxy (**An-MCz**), or methoxyethoxy (**An-ECz**) groups linked to C-3 and C-6 positions of carbazole moieties exhibited a double-waved reversible oxidation−reduction pattern between 0.00 and 0.97 V (over three repeated scans). Oxidation onsets were observed at 0.68, 0.45, and 0.46 V (vs Fc/Fc+), the peaks of the first waves were recorded at 0.78, 0.55, and 0.56 V, and those of the second waves were observed at 0.97, 0.96, and 0.98 V. No reduction waves were observed down to −2.0 V. The ionization potentials (IP_{CV}) of the target compounds were derived using the following equation: IP_{cv} (eV) = $-E_{ox}$ (V) − 4.8.[47] The calculated IP_{CV} values for the new derivatives fell in the range of 5.25−5.48 eV. Compared to the *tert*-butylated derivative (**An-tBCz**), alkoxy group-containing compounds (**An-MCz** and **An-ECz**) showed lower IP_{CV} values by 0.22−0.23 eV. These results correlate well with previous findings.[48]

Ionization potentials of the solid samples of the compounds (IP_{PE}) were measured by photoelectron emission spectroscopy. The electron photoemission spectra are shown in Figure 2b. The IP_{PE} values are collected in Table 2. These values were derived from the linear segments of the spectra, specifically at the points where the photocurrent was zero.

The ionization energy was altered by the interaction of ionized molecules with the solid, polarizable surroundings, affecting the polarization energy. The IP_{PE} values exceeded the IP_{CV} values (Table 2), likely because of enhanced intermolecular interactions (hydrogen bonding). For anthracene derivatives (**An-MCz** and **An-ECz**), which contain alkoxy groups, the IP_{PE} values were 0.1−0.2 eV lower than the IP_{PE} value of the compound with the *tert*-butylated carbazole moiety (**An-tBCz**).

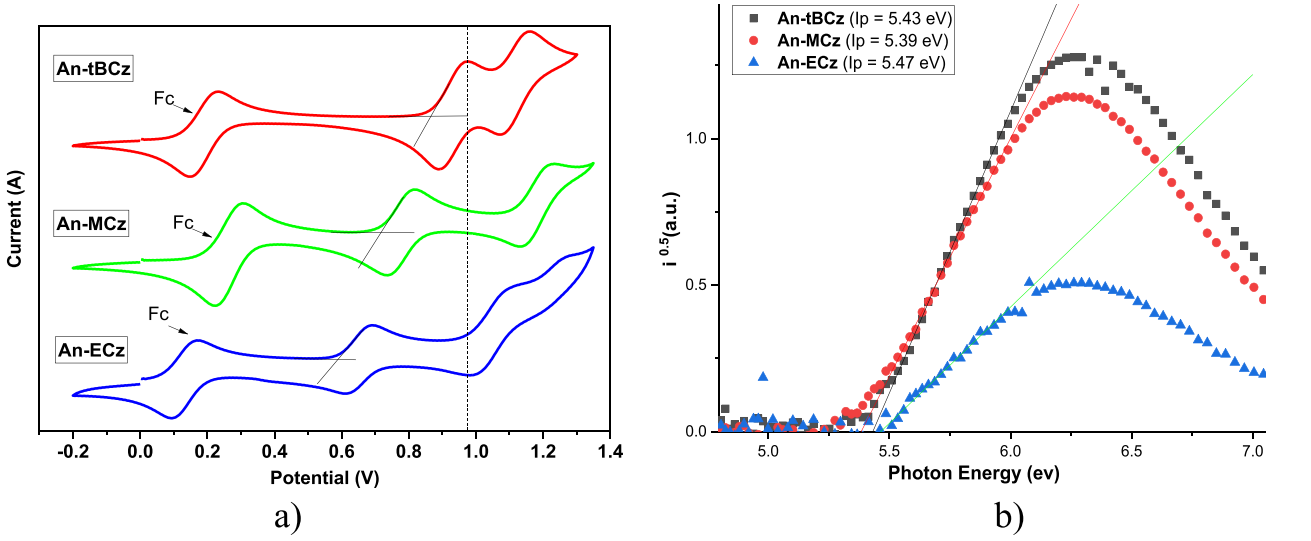

Figure 2. Cyclic voltammetry curves of DCM solutions (a) and photoelectron emission spectra of the layers (b) of **An-tBCz**, **An-MCz**, and **An-ECz**.

https://doi.org/10.1021/acsaelm.4c00533
ACS Appl. Electron. Mater. 2024, 6, 4489−4503

Table 2. Electrochemical Characteristics of Compounds An-tBCz, An-MCz, and An-ECz[a]

compound	E_{ons} (V)	$E_{ox,pa}$ (V)[b]	$E_{ox,pc}$ (V)[b]	IP_{cv} (eV)[c]	E_g (eV)[d]	EA_{PE} (eV)[e,f]	IP_{PE} (eV)[f]	LUMO (eV)[g]	HOMO (eV)[g]	E_{gap} (eV)[g]
AN-tBCz	0.68	0.78/0.97	0.70/0.89	5.55	2.92	2.51	5.43	1.97	5.27	3.29
AN-MCz	0.45	0.55/0.96	0.48/0.88	5.23	2.89	2.5	5.39	1.97	4.95	2.98
AN-ECz	0.46	0.56/0.98	0.49/0.86	5.24	2.79	2.68	5.47	1.96	5.01	3.05

[a]Data values were calibrated with the ferrocene (Fc) standard. [b]E_{ox}^{pa}, E_{ox}^{pc}—peak potentials corresponding to successive molecular first and second oxidations, respectively. [c]$IP_{cv} = -1.4E_{onset,ox}$ (V) − 4.6. [d]Estimated from the onset of absorption spectra of the films. [e]Calculated using E_g values. [f]Estimated from photoelectron emission spectra in air. [g]Evaluated from theoretical calculations.

Table 3. Bond Angle 1 (θ_1) and Bond Angle 2 (θ_2), REs for Electron and Hole Transport, and Dipole Moments (D) in the Gas State and Solutions of An-TBCz, An-MCz, and An-ECz

compound	θ_1 (deg)	θ_2 (deg)	λ_e (eV)	λ_h (eV)	D (gas)	D (toluene)	D (THF)
An-tBCz	85.5	52.5	0.5329	0.1838	4.13	4.48	4.67
An-MCz	79.4	51.7	0.4796	0.1898	4.79	5.09	5.25
An-ECz	78.9	51.6	0.4688	0.2004	5.34	5.65	5.81

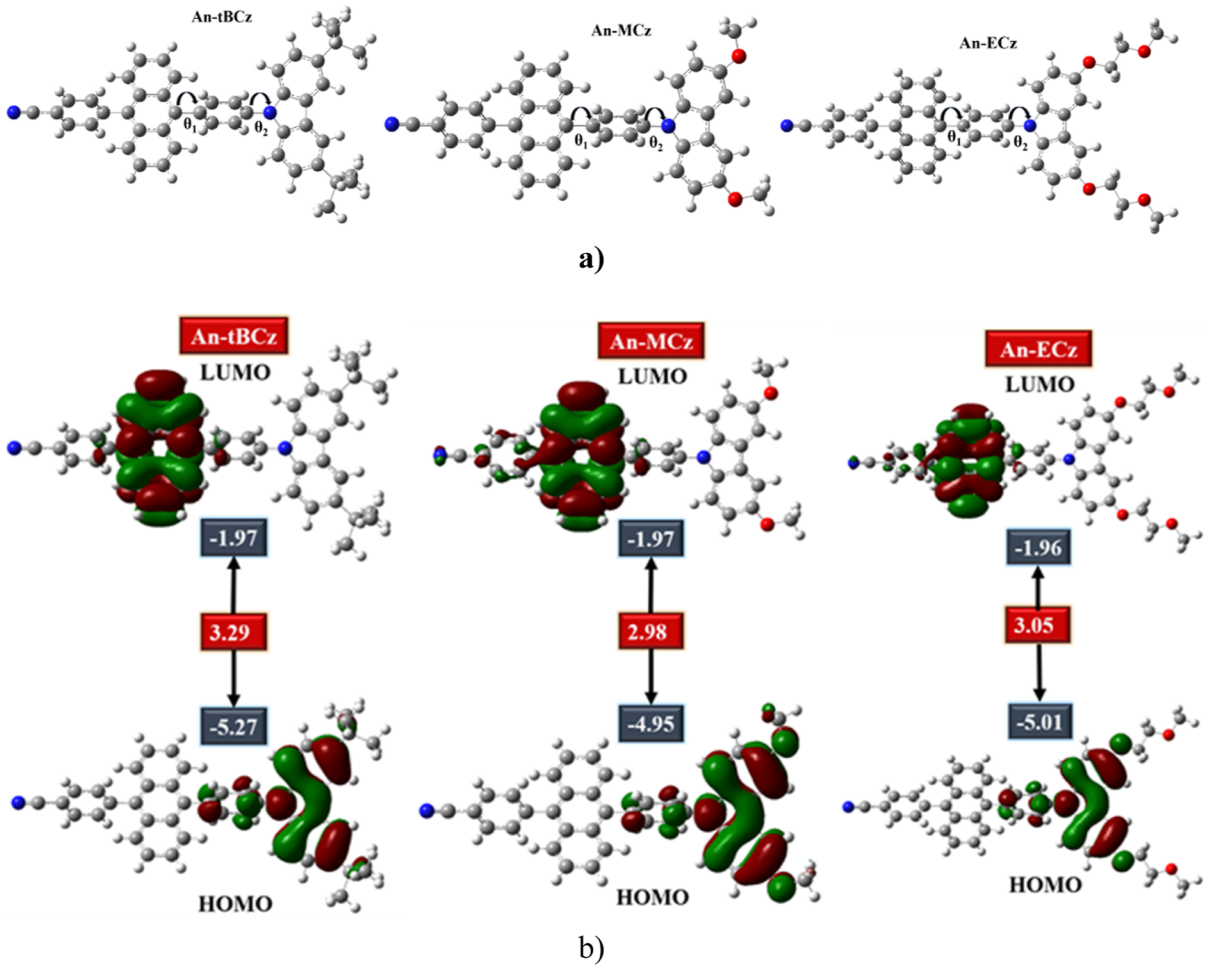

Figure 3. Optimized geometries (a) and molecular orbitals with energy levels of **An-tBCz**, **An-MCz**, and **An-ECz** (b) at B3LYP/6-31G(d,p).

Theoretical Calculations. The dihedral angles between anthracenyl benzonitrile and the phenyl present in the core (dihedral angle 1, θ_1) and between the carbazole moiety and the phenyl present in the core (dihedral angle 2, θ_2) were calculated. The values are given in Table 3. θ_1 is wider than θ_2 for all the studied compounds, indicating that the donor and acceptor parts of the molecules are nonplanar with the possibility of charge separation between the donor and acceptor (Figure 3a).

The highest occupied and lowest unoccupied molecular orbitals (HOMO and LUMO, respectively), together with their respective energy levels and theoretical band gaps (E_{gap}), are shown in Figure 3b and Table 2.

Carbazole and its *tert*-butyl substituents in **An-tBCz**, carbazole and its methoxy substituents in **An-MCz**, and carbazole and part of its methoxyethoxy substituents in **An-ECz** are the main sites of charge density existence in the HOMO, deciphered as the donor part of the molecules. Since the dihedral angles between the carbazole moieties and the

https://doi.org/10.1021/acsaelm.4c00533
ACS Appl. Electron. Mater. 2024, 6, 4489−4503

Table 4. Major Photophysical Characteristics of the Compounds

compound	λ_{max} (nm)	Φ (%)	λ_{max} (nm)	Φ (%)	S_1[a] (eV)	T_1 (eV)	ΔE_{ST} (eV)	S_1 (eV)	T_1 (eV)	ΔE_{ST} (eV)
	deox. tol.		film		film, Argon, 77 K			theor.		
An-tBCz	439	76	454	17		no data	ca. 1	2.93	1.74	1.20
An-MCz	452	95	480	24	2.93	1.92	1.01	2.64	1.73	0.91
An-ECz	454	99	493	37	2.86	1.89	0.97	2.70	1.73	0.97

[a]^{1}CT.

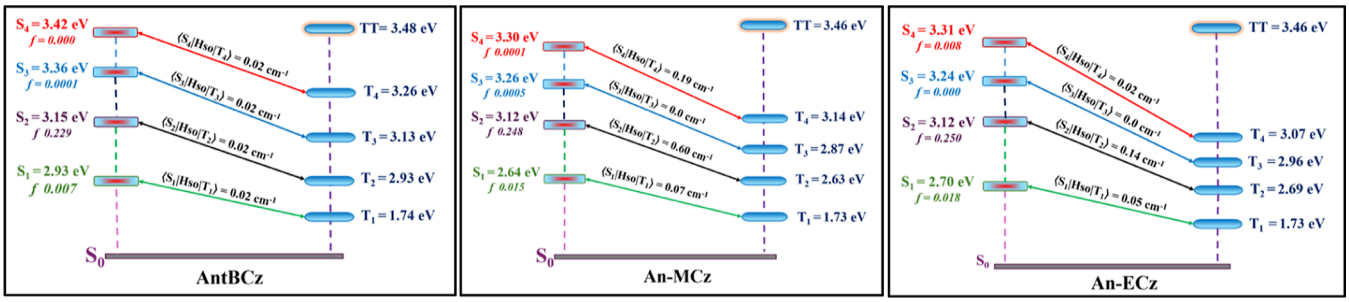

Figure 4. Energy level diagram of the first four singlet and triplet states, oscillator strength (f), and spin−orbit coupling matrix of **An-TBCz**, **An-MCz**, and **An-ECz**.

phenyl group in the centers of the molecules are not very high, the charge density is also placed on the central phenyl groups in the HOMO state. The charge density is situated on anthracenyl benzonitrile in the LUMO of all molecules studied; anthracenyl benzonitrile moieties are identified as the acceptor parts of the molecules due to the existence of highly electronegative nitrile substituents at the terminal parts. The charge separation in the HOMO and LUMO can be clearly evaluated from high θ_1 and the phenyl group in the core of the molecules acting as a bridge between the substituted carbazole moieties as the donor parts and anthracenyl benzonitrile moieties as the acceptors. **An-tBCZ** has the most stable HOMO since it is characterized by the lowest HOMO energy (−5.27 eV).[49] **An-MCz** and **An-ECz** have comparable stability of the HOMO because of their comparable HOMO energy levels (−4.95 and 5.01 eV, respectively). The calculated HOMO−LUMO E_{gap} (Table 2) corresponds to the optical band gap E_g calculated from the onset of the absorption spectra of toluene solutions to a great extent for every compound.

Time-dependent DFT (TD-DFT) calculations were also performed at B3LYP/6-31G(d,p) up to 30 excited states for the investigated compounds in the gaseous phase. The impact of solvent was also computed using the integral equation formalism polarizable continuum model (IEFPCM). The computed absorption spectra of **An-tBCz**, **An-MCz**, and **An-ECz** in the gas phase and toluene and tetrahydrofuran (THF) solutions along with the comparison of empirical absorption spectra of these compounds are shown in Figure S7. The TD-DFT results for the compounds in the gaseous phase are given in Table S1, and those for toluene solutions are given in Table S2. The theoretical absorption trends of compounds in the gas phase and in both solutions are potentially correlated with the experimental absorption spectra. For example, in the experimental absorption spectrum of the dilute solutions of the compounds in toluene, the first peak of **An-tBCz** from *tert*-butylated carbazole at 296 nm corresponds to the computed absorption band for **An-tBCz**, with the transition of $S_0 \rightarrow S_8$ at the wavelength of 306 nm and oscillator strength (f) of 0.322. In the empirical absorption spectrum of **An-MCz**, the peak of the methoxy-substituted carbazolyl group was found at 310 nm. In the case of **An-ECz**, the peak of the methoxyethoxy-substituted carbazole moiety was observed at 311 nm. The $S_0 \rightarrow S_8$ transition in the theoretical spectrum of **An-MCz** corresponds to the wavelength of 324 nm and f of 0.28. The $S_0 \rightarrow S_8$ transition in the case of **An-ECz** is related to the intense peak at 319 nm with an f value of 3.88. The experimental absorption trend of multiple peaks from anthracenyl benzonitrile remains almost the same for all the molecules (**An-tBCz**, **An-MCz**, and **An-ECz**). The second intensive peaks observed in the computed absorption spectra correspond to transition $S_0 \rightarrow S_2$ (167 → 169) manifesting at 396 nm with an f of 0.26 for **An-tBCz**, to transition $S_0 \rightarrow S_2$ (151 → 153) manifesting at 401 nm with an f of 0.28 for **An-MCz**, and to transition $S_0 \rightarrow S_2$ (175 → 177) manifesting at 400 nm with an f of 0.28 for **An-ECz**. It illustrates good agreement of theoretical and empirical absorption aspects. The overall absorption trends for all of the compounds remained the same for toluene and THF solutions. A slight red shift (Figure S7) compared to the signature band of carbazole was also observed in the computed first absorption peak from the carbazole moiety of the molecules in the gas phase, which may be caused by the self-polarity and self-assembly of the carbazole-based moiety that causes self-excitation.[50,51] The theoretical estimations of S_1 and T_1 energies corresponding to the empirical singlet and triplet state energies of **An-MCz** and **An-ECz** calculated at 77 K with excitation at 300 nm support the potential charge transfer energies and the existence of an infrared peak (Tables 4 and S1). The computed S_1 energy of **An-tBCz** (2.93 eV) illustrates the charge transfer energy of the molecule. The theoretical T_1 energy of 1.74 eV supports the potential existence of vibronic sublevel peak in the spectrum of **An-tBCz**. The energies of the first four singlet (S_1−S_4) and first four triplet states (T_1−T_4), along with the calculated spin−orbit interaction (H_{so}) between them, for **An-TBCz**, **An-MCz**, and **An-ECz** are illustrated in Figure 4. Spin−orbit coupling matrix elements (SOCMEs) for S_1−S_4 with T_1−T_4 were computed in detail (Table S3). They illustrate an extremely small SOCME between these states (less than 1 cm^{-1}). The observation of such weak SOCMEs indicates the

https://doi.org/10.1021/acsaelm.4c00533
ACS Appl. Electron. Mater. 2024, 6, 4489−4503

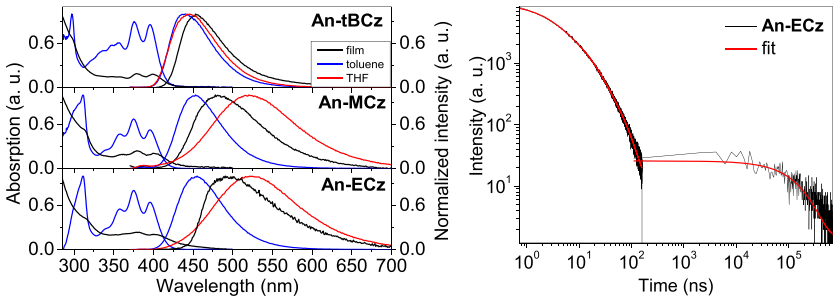

Figure 5. Absorption and PL spectra (a) of toluene and THF solutions and of the films of the compounds recorded at room temperature and PL decay curves (b) of the film of **An-ECz** recorded in vacuum at room temperature. PL decay curves were recorded at an emission wavelength of 493 nm in ns and ms ranges using laser PicoQuint and xenon lamp μF2 as the excitation sources at an excitation wavelength of 374 nm.

least probability of RISC and ISC. However, it implies a heightened likelihood of TTA.

Applying the Marcus theory to the analysis of the RE allows one to probe the degree of charge mobility on intermolecular and intramolecular scales.[52] Internal and external REs combine to form the total RE. In external RE, polarization changes occur during charge transfer, and the external environment undergoes rapid variations, while the structural variation of a molecule is the key factor in internal RE.[53] We focused only on the internal RE for the purpose of our study because external RE cannot be computed from various external aspects. The numerical values were calculated using eqs 1 and 2 (Table 3)[54,55]

$$\lambda_h = [E_+^0 - E_0] + [E_0^+ - E_+] \quad (1)$$

$$\lambda_e = [E_-^0 - E_0] + [E_0^- - E_-] \quad (2)$$

The optimized neutral molecules with energies of the cation and anion are E_0^- and E_0^+, respectively. The anions and cations, optimized with anion and cation energies, are E_- and E_+, respectively. The optimized anion and cation with neutral energies are E_+^0 and E_-^0, respectively. The RE studies show that the investigated molecules exhibit highly efficient hole transport compared with electron transport. **An-tBCz** with the smallest λ_h possessing the highest hole mobility is due to its alkyl substituted carbazole donor unit. **An-MCz** with a methoxy-substituted carbazole donor moiety was characterized by the second highest hole mobility. **An-ECz** showed the lowest hole mobility among the investigated compounds. These observations show that the attachment of methoxy and methoxyethoxy substituents to the carbazole moiety results in the slightly decreasing hole mobilities of the derivatives of carbazole and anthracene. **An-ECz** containing a methoxyethoxy-substituted carbazole unit exhibited the best electron mobility. The dipole moments calculated for the excited states in the gas phase and toluene and THF solutions showed a slight increase going from the gas phase to toluene solution and a slight increase for THF solution compared to that of toluene solution (Table 3). This illustrates the polarization impact of polar solvents. This also supports the phenomenon of solvatochromism for **An-MCz** and **An-ECz** owing to the red shift in their emission in THF as compared to the emission in toluene. The dipole moment of **An-tBCz** is the lowest in all environments. The dipole moments of alkoxy derivatives (**An-MCz** and **An-ECz**) are considerably higher.

DOS analysis was performed to better understand the participation of different units of the molecules (donor, bridge, and acceptor) in the HOMO and LUMO.[56] Determining the configurations of Frontier molecular orbitals (FMOs) in relation to Mulliken charge density relies heavily on DOS calculations.[57] To understand the participation of several molecular units in the FMOs, we regarded the *tert*-butyl-, methoxy-, and methoxyethoxy-substituted carbazole fragments in **An-tBCz**, **An-MCz**, and **An-ECz**, respectively, as the donor moieties. The phenyl ring in the core as the bridge and anthracenyl benzonitrile are regarded as the acceptors. In the DOS plots of **An-tBCz**, **An-MCz**, and **An-ECz** (Figure S8), the *x*-axis represents the energy, the *y*-axis represents the relative intensity, and the black, red, and green lines show the levels of participation of donor, bridge, and acceptor units in FMOs, respectively. The total participation is shown by the blue line. The numerical participation information is given in Table S4. The trend of the participation of the different units in the FMOs is almost the same for all of the molecules investigated. DOS analysis indicated a level of donor at ca. 90%, a level of bridge up to 10%, and a slight involvement of the acceptor of ca. 1% in the HOMO. In the LUMO, a major participation of 98.6−99% is shown by the acceptor unit, a very slight involvement of that of the bridge, and negligible participation by the donor of no more than 0.1%. DOS analysis provides a clear evaluation of θ_1 and θ_2, as well as the presence of charge density in the FMOs, as shown in Figure 3a, via the sequential operation of the phenyl unit as a bridge.

Photophysical Properties. Absorption spectra of toluene solutions of the compounds (Figure 5a) consist of the signature absorption peaks of carbazole at a wavelength shorter than 350 nm and vibronic multipeak bands of anthracene in the longer wavelength range.[58,59] The carbazole-related absorption band of the low-energy $\pi-\pi^*$ transition around 300 nm is bathochromically shifted for **An-MCz** and **An-ECz** when compared to that for **An-tBCz** due to the attachments of alkoxy substituents to the carbazole moieties notably increasing π-conjugation.[60] The anthracene-based vibronic bands are located almost at identical wavelengths for all the investigated compounds. These bands are red-shifted by ca. 25 nm from the previously reported position for anthracene absorbance. This observation is explained by the addition of a benzonitrile moiety to the acceptor, expanding π-conjugation.[61] The absorption spectra of the films are broader and red-shifted in comparison to those of the corresponding toluene solutions because of the enhanced intermolecular interactions in the solid state.

PL spectra contain single peaks and show the occurrence of positive solvatochromism for **An-MCz** and **An-ECz**. It

https://doi.org/10.1021/acsaelm.4c00533
ACS Appl. Electron. Mater. 2024, 6, 4489−4503

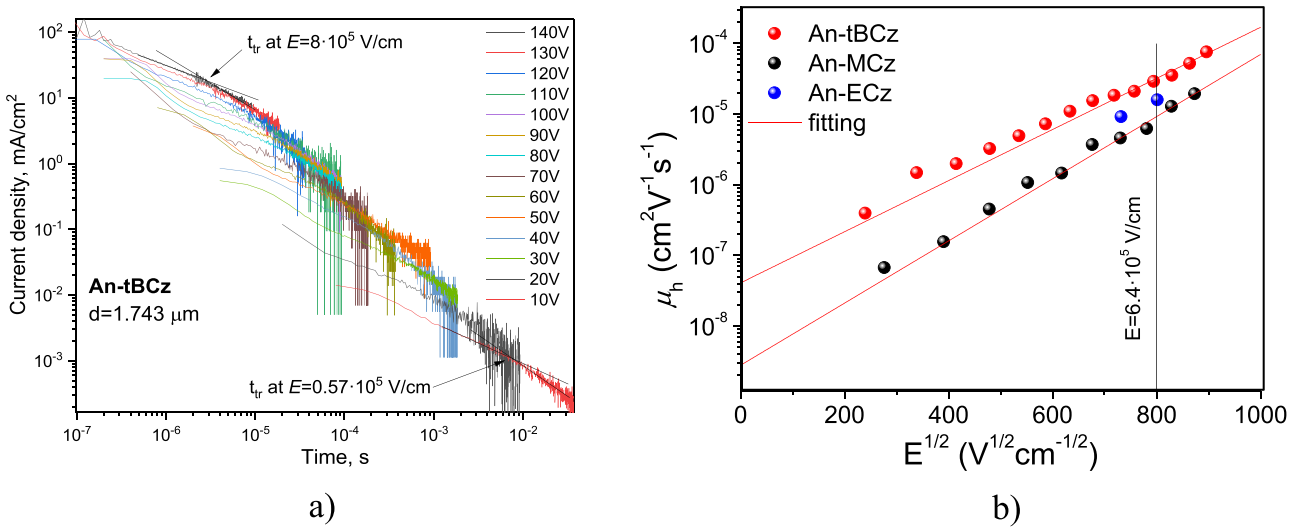

Figure 6. TOF signals (a) for holes recorded for the vacuum-deposited film of **An-tBCz** at different electric fields and hole mobilities (μ_h) of **An-tBCz**, **An-MCz**, and **An-ECz** (b) plotted as a function of electric fields according to the Poole−Frenkel relationship.

manifests by the red shift of emission of the solution when the nonpolar toluene is changed by the polar THF. The apparent solvatochromic effect highlights the intramolecular charge transfer (CT) between the alkoxy-substituted carbazole and 4-(anthracene-9-yl)benzonitrile. Thus, the emission of **An-MCz** and **An-ECz** at room temperature is associated with radiative deactivation of excitons from the ^{1}CT state. The ^{1}CT peak is shifted to the red spectral range for **An-MCz** and **An-ECz** when compared to the emission of **An-tBCz** (Figures 5a and S9b) suggesting ^{1}LE emission of the local excited (LE) state of anthracene for **An-tBCz**. The peaks of PL bands in the films of the compounds are situated in between the peaks of the PL bands of toluene and THF solutions, highlighting the self-polarity of the layers, which are less polar than THF. The highest Φ values were observed for deoxygenated toluene solutions and the films of compound **An-ECz** containing methoxyethoxy-substituted carbazole fragments. They were found to be of 99 and 37%, respectively (Table 4). Compound **An-MCz** having methoxy-substituted carbazolyl groups showed slightly lower values of Φ, while the solutions and films of **An-tBCz** showed the least efficient emission. The significantly lower Φ shown by the solid films can be explained in terms of aggregation-caused quenching or PL quenching by interception of the triplet electronic excitation energy by collisional interactions of the molecules and oxygen.[62] The utilization of triplet excited states in emissive processes is confirmed by the PL decay curves of the films of **An-MCz** and **An-ECz** (Table S5 and Figures 5b and S9a). The films of all of the investigated compounds have sub-10 ns lifetime components of the PL decay curves assigned to prompt fluorescence. Additionally, PL decay curves of **An-MCz** and **An-ECz** have components with the lifetimes of ca. 30 ns and 0.15 ms. The removal of oxygen did not change the spectral profile of the emission of the films at room temperature. Thus, the spectral contribution of the triplet energy is from the same excited states as those for prompt fluorescence. This observation allows us to exclude RTP from the origin of the emission. Consequently, the long-lived PL of **An-MCz** and **An-ECz** is attributed to delayed fluorescence.

Time-resolved PL spectra were recorded for the films of the compounds at 77 K (Figure S9d). **An-tBCz** exhibited a double peak PL band that cannot be interpreted indisputably with a cutoff energy of 2.94 eV assigned to ^{1}LE. The origin of the second subpeak can be in the presence of vibronic sublevels, emission of the ^{1}CT state at a lower energy than for the ^{1}LE or the DF energized by TTA. The PL spectrum of the film of **An-tBCz** recorded with a delay of 0.1 ms is not very intensive to correctly evaluate the onset energy and the position of the peaks that would help make an appropriate description of its nature. **An-MCz** has a ^{1}CT peak at 2.92 eV. Both **An-MCz** and **An-ECz** exhibit an infrared peak at ca. 730 nm, appearing if excited at 300 nm but not at 350 nm. The cutoff energy of the band fits the theoretical prediction of the energy level position for T_1 (Table 4). The existence of the emission with a long lifetime is evident from the spectrum of the film of **An-ECz** recorded at 77 K with the delay. The intensity of the band is high when excited at 300 nm. At an excitation wavelength of 350 nm, the anthracene moiety is excited directly, causing enhancement of TTA. Consequently, the electronic excitation energy from T_1 is used in TTA and is not deactivated through radiative recombination via phosphorescence. The extension of the donor in the structure resulted in a lowering of the T_1 energy level from 1.92 for **An-MCz** to 1.89 eV for **An-ECz**. The energy level of T_1 for **An-tBCz** is assumed to be close to those of other compounds of the series as the state is identified as of LE origin. The PL spectra recorded without delay exhibit the difference in the energy levels of the major low-energy PL peak for **An-ECz** when excited at different excitation wavelengths. The peaks are assigned to ^{1}LE and ^{1}CT, with estimated cutoff energy levels of 3.01 and 2.86 eV, respectively. The spectrum recorded with the excitation wavelength of 300 nm has a ^{1}CT peak, which is in total correspondence with its location when compared to the spectra of **An-MCz** recorded both at 77 K and at room temperature (Figure S9). The observed spectral behavior is determined by TTA. The discussed enhancement of TTA when the anthracene is excited directly provides energy to the ^{1}LE state, which is higher than that of ^{1}CT and closer to the energy of $2{\cdot}T_1$ (Table 1 and Figure S9b). Thus, the ^{1}LE emission of the film of **An-ECz** is delayed fluorescence caused by TTA. It is observable in the PL spectra recorded with the delay. The bands of long-lived emission in these spectra correlate with the position of

https://doi.org/10.1021/acsaelm.4c00533
ACS Appl. Electron. Mater. 2024, 6, 4489−4503

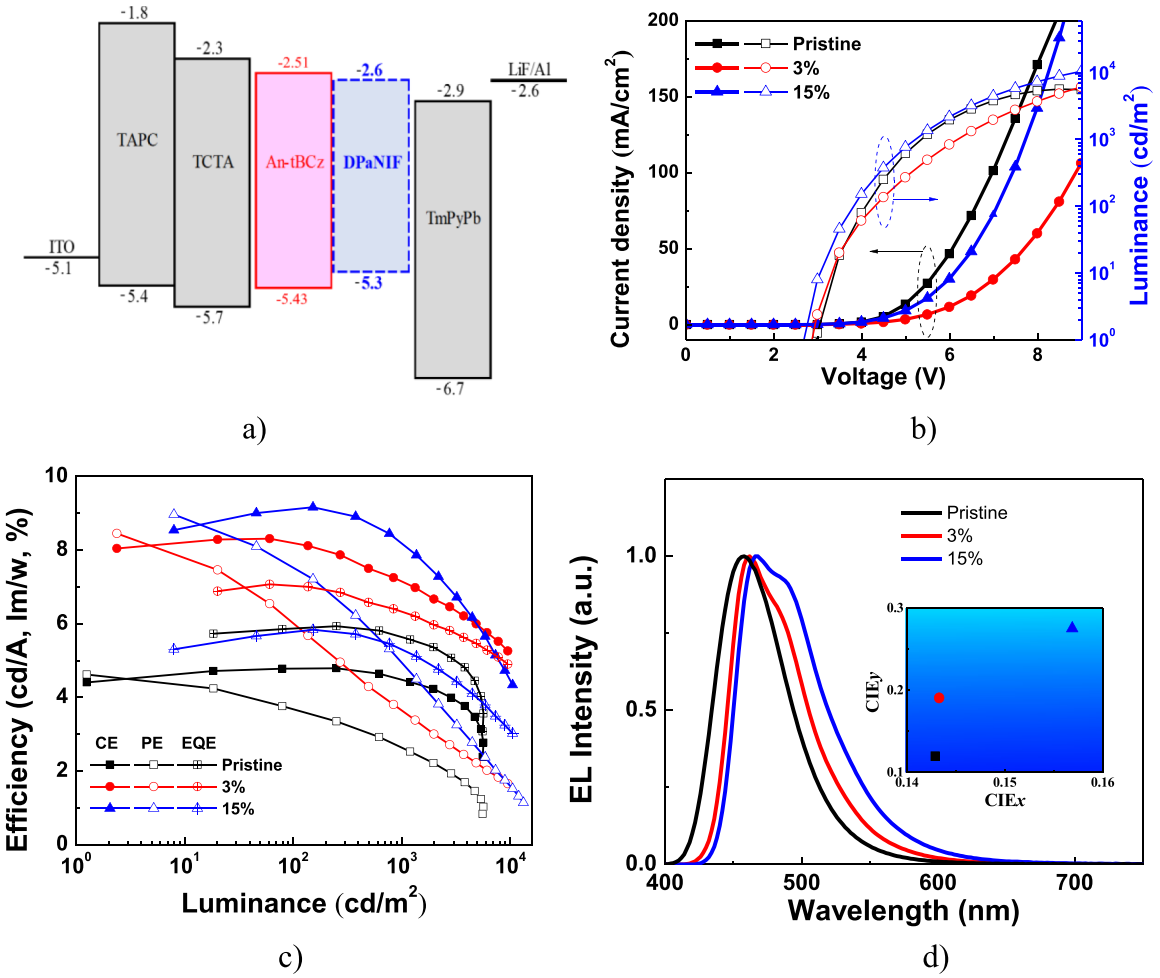

Figure 7. (a) Device structure and energy levels of each layer, (b) J−V−L curves, (c) η_{CE}, η_{PE}, and η_{EQE} vs L curves, and (d) EL spectra and 1931 CIE color coordinates recorded at 5 V of OLEDs with the EML of **An-tBCz** and 3 and 15% concentrations of DPaNIF in **An-tBCz**.

^{1}LE. The film of **An-TBCz** does not exhibit any peak of phosphorescence (Figure S9d). No long-lifetime component (in the millisecond range) is observed in the PL decay curves (Figure S9a). These observations are interpreted as a suppressed accumulation of triplet energy on T_1 needed for both phosphorescence and TTA, meaning that the main path of deactivation of the T_1 state is nonradiative conversion to the ground state. The values of the energy of the excited states estimated from experimental data and theoretical calculations are in good agreement (Table 4).

Charge Transport Properties. The TOF method allows the selective measurement of transit times (t_{tr}) of holes or electrons in thick semiconductor layers by applying the positive or negative voltages (V) to the optically transparent electrode.[63] We applied TOF for vacuum-deposited layers of **An-tBCz**, **An-MCz**, and **An-ECz** using a sample configuration of indium tin oxide (ITO)/thick layer/Al (Figures 6 and S10). The d values of organic layers of **An-tBCz**, **An-MCz**, and **An-ECz** were determined by the profilometer Profilm3D (Figure S11). The high dispersity of hole transport was observed for layers of all the studied compounds. The t_{tr} values were identifiable at the cross point of two lines (shown by the arrows) by analyzing the log−log plots of the TOF signals (Figures 6a and S11). As can be expected for organic semiconductors, holes in **An-tBCz** exhibited smaller t_{tr} values at lower electric fields (E), while faster hole transport was detected at higher E (Figure 6a). No electron transport was detected in the layers of **An-tBCz**, **An-MCz**, and **An-ECz** (Figure S10).

Collecting t_{tr} values at the different E, hole mobilities (μ_h) were calculated for the layers of **An-tBCz**, **An-MCz**, and **An-ECz** using the formula $\mu_h = d^2/(V \times t_{tr})$. Figure 6b shows plots of μ_h as a function of electric fields in accordance with the Poole−Frenkel relationship $\mu_h = \mu_{0h} \exp \beta E^{1/2}$. Here, μ_{0h} and β have a common meaning of μ_h at zero electric field and Poole−Frenkel electric field dependence, respectively. For **An-tBCz** and **An-MCz**, μ_{0h} of 4.09×10^{-8} and 2.79×10^{-9} cm^2 V^{-1} s^{-1} and β of 8.33×10^{-3} and 10.1×10^{-3} cm$^{1/2}$ V$^{-1/2}$, respectively, were obtained by fitting using the Poole−Frenkel formula (Figure 6b). **An-tBCz** showed the highest μ_h of 3.17×10^{-5} cm^2 V^{-1} s^{-1} at an E of 6.4×10^5 V·cm^{-1}. Meanwhile, at the same E value, **An-MCz** showed a μ_h of 1.6×10^{-5} cm^2 V^{-1} s^{-1} and **An-ECz** showed 8.84×10^{-6} cm^2 V^{-1} s^{-1}. The differences of hole mobility parameters of the compounds could be explained by the different molecular packing causing different HOMO−HOMO overlapping and different energetic disorder parameters. This statement is in good agreement with the theoretical predictions described above showing the lowest λ_h of 0.1838 eV, thus the best hole mobility for **An-tBCz** (Table 3). The TOF measurements prove that **An-tBCz** is the most potential candidate for use in electronic devices.

https://doi.org/10.1021/acsaelm.4c00533
ACS Appl. Electron. Mater. 2024, 6, 4489−4503

Table 5. Characteristics of Blue TTA-Based OLEDs with the EML of Pure An-tBCz and of Its 3 and 15% Molecular Mixtures with DPaNIF

EML	V_{ON}[a] (V)	η_{CE}[b] (cd·A^{-1})	η_{PE}[b] (lm·W^{-1})	η_{EQE}[b] (%)	L at 9 V (cd·m^{-2})	λ_{peak} (nm)	1931 CIE$_{x,y}$	fwhm (nm)
Doping-Free EML:TTA Emitter An-tBCz								
An-tBCz	3.7/2.9	4.8/4.5	4.2/2.7	5.9/5.6	5578	458	(0.143, 0.120)	60
TTA-Assisted Hyperfluorescent EML: DPaNIF (x wt %): An-tBCz								
An-tBCz + 3% of DPaNIF	4.1/2.7	8.3/7.2	7.5/3.7	7.1/6.3	6116	462	(0.143, 0.191)	59
An-tBCz + 15% of DPaNIF	3.7/2.5	9.2/8.2	9.0/5.0	5.9/5.3	10,500	466	(0.157, 0.275)	69

[a]Voltage at 1 mA·cm^{-2} and 1 cd·m^{-2}. [b]Recorded at maximum and 1000 cd·m^{-2}.

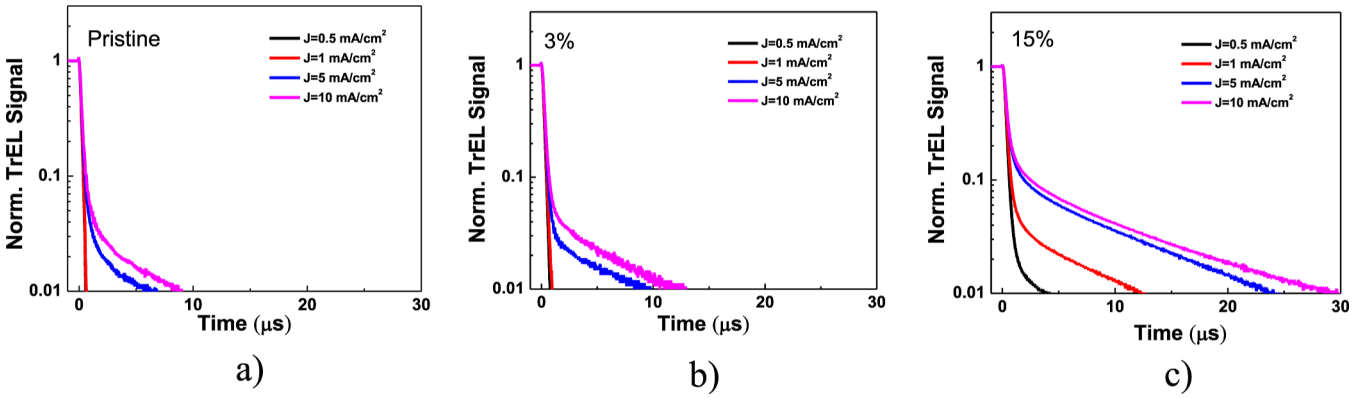

Figure 8. Transient EL signals of OLEDs with the different EMLs: (a) pure **An-tBCz**, (b) 3% of DPaNIF in **An-tBCz**, and (c) 15% of DPaNIF in **An-tBCz** recorded under various driving J of 0.5, 1, 5, and 10 mA cm^{-2}.

Electroluminescence Properties. **An-tBCz**, was employed as the emitter and host of the emitting layer (EML) inside blue TTA-based doping-free and TTA-assisted hyperfluorescent OLEDs. The detailed OLED structure and energy levels are listed in Figure 7a. Two hole transport layers 4,4′-cyclohexylidenebis[*N*,*N*-bis(4-methylphenyl)benzenamine] (TAPC) and tris(4-carbazoyl-9-ylphenyl)amine (TCTA), an EML consisting of **An-tBCz** and a blue fluorescence emitter 7,7,13,13-tetramethyl-N5,N5,N11,N11-tetraphenyl-7,13-dihydrobenzo-[*g*]indeno[1,2-*b*]fluorene-5,11-diamine (DPaNIF), an electron transport layer of 1,3,5-tri(*m*-pyridin-3-ylphenyl)-benzene (TmPyPb), an electron injection layer of lithium fluoride (LiF). and a highly reflective aluminum (Al) cathode were used in the fabrication of OLEDs. The thickness of the layer of TAPC was 40 nm; for the layer of TCTA, it was 10 nm; for EML, it was 17.5 nm; for the layer of TmPyPb, it was 40 nm; for the layer of LiF, it was 1 nm, and the thickness of the Al layer was 100 nm. Three devices were fabricated by varying the composition of the EML. In one device, an EML of pristine **An-tBCz** was used, in the second one, an EML of 3% molecular dispersion of DPaNIF in **An-tBCz** was used, and in the third one, an EML of 15% molecular dispersion of DPaNIF in **An-tBCz** was used. The dopant concentration of the EML was optimized well to obtain maximum η_{CE} and η_{EQE} (Table S6 and Figure S12). The EL characteristics of these three blue TTA-based OLEDs are shown in Figure 7b–d. They include current density–brightness–voltage (J–L–V) plots, plots of η_{CE}, η_{PE}, and η_{EQE} versus L, normalized EL spectra, and color coordinates at 5 V. The parameters are summarized in Table 5. The turn-on voltages at J = 1 mA cm^{-2} of these three devices are in the range of 3.7–4.1 V. Their lit-on voltages at L of 1 cd m^{-2} are in the range of 2.5–2.9 V. The device with the EML of pure **An-tBCz** exhibits relatively high lit-on voltage due to the large energy band gap of emitter **An-tBCz**, resulting a shorter wavelength EL spectrum with a peak wavelength (λ_{peak}) of 458 nm and a bluer color coordinate of (0.143, 0.120). This deep-blue emitting device also shows high maximum current efficiency η_{CE}, power efficiency η_{PE}, and η_{EQE} of 4.8 cd A^{-1}, 4.2 lm W^{-1}, and 5.9%, respectively. Taking into account the rather low Φ value of the film of the emitter, this η_{EQE} value is rather high. It is higher than the limit EQE of OLEDs based on prompt fluorescence of 5%,[18,64] implying the TTA mechanism to be responsible for the exploitation of triplet excitons in the emission. The limit is set according to the equation $\eta_{EQE} = \gamma \times \Phi \times \chi \times \eta_{out}$ as the OLEDs based on prompt fluorescent emitters are characterized by the maximum formation of the exciton used in EL limited by the IQE at 25%.[18,64] γ is the charge balance factor, and η_{out} is an out-coupling factor.

Notably, the device with the emitting layer of pure **An-tBCz** shows an excellent efficiency roll-off of ca. 5% in η_{EQE} while it is operated at an L of 1000 cd m^{-2}. With DPaNIF dopant, the devices show enhanced η_{CE} and η_{PE}, as well as a green shift of the EL spectrum (Table S7 and Figures S12 and S13). In addition, the Φ of the **An-tBCz** film doped with 3% DPaNIF is 61.3%. This observation indicates efficient exciton energy transfer from host **An-tBCz** to the emitter DPaNIF. The HOMO and LUMO energy levels of the host and guest compounds have perfect alignment with each other and with those of the compounds of the transporting layers (Figure 7a), thus improving the charge balance and energy transfer. However, the low concentration (3%) of the emitter in the **An-tBCz** matrix results in relatively low L and rather high turn-on voltage. The turn-on and lit-on voltages (at 1 mA cm^{-2} and 1 cd m^{-2}, respectively) are reduced by rising dopant concentration. Hence, the OLED with 15% concentration of DPaNIF in the EML exhibits max. η_{CE}, η_{PE}, and L at 8.5 V of 9.2 cd A^{-1}, 9.0 lm W^{-1} and 10,500 cd m^{-2}, respectively. However, the EL spectrum shows the obvious green color coordinates of (0.157, 0.275), a λ_{peak} of 466 nm, and a wide bandwidth due to the microcavity resonant effect inside the

https://doi.org/10.1021/acsaelm.4c00533
ACS Appl. Electron. Mater. 2024, 6, 4489–4503

device. These variations in EL spectra show that the carrier recombination zone shifts with the increasing dopant concentration toward the HTL and broadens inside the EML. At the same time, the η_{EQE} decreases due to concentration quenching. The values of full width at high maximum (fwhm) of the OLEDs with lower concentrations are smaller than 60 nm, similar to previously reported devices exhibiting TTA (Table 5).[26,28]

To verify the TTA mechanism of **An-tBCz**-based OLEDs, time-resolved electroluminescence (TrEL) measurements were performed for the aforementioned three devices by varying pulsed driving J (of 0.5, 1, 5, and 10 mA cm^{-2}, respectively). Figure 8 shows the TrEL signals of the three devices. TTA is manifested from the increase in intensity of long-lived emission at high driving J. The increased number of triplets results in the increase of the probability of two triplets meeting together to induce TTA. After the addition of the DPaNIF dopant, the TrEL signals exhibit a longer-lived delayed emission than the TREL of the OLED with the EML of pure **An-tBCz**. This observation indicates that the fluorescent emitter facilitates the TTA process of the **An-tBCz** host, especially in the case of the OLED with the EML containing 15% DPaNIF.

The additional series of OLEDs with the different nonoptimized structures based on the doping-free and guest−host EML were fabricated using **An-tBCz**, **An-MCz**, and **An-ECz** specifically to detect the manifestation of TTA without the aim of achieving satisfactory efficiency or device stability. TTA is a process of the annihilation of two triplet excitons. The delayed fluorescence resulting from TTA has kinetic regimes of low and high annihilation.[65,66] At the low regime, the correlation between the intensities of delayed fluorescence and excitation is quadratic until the TTA becomes saturated. The dependence becomes linear at the kinetic regime of saturated TTA. This relation corresponds to the slopes of 2 at low J and of 1 at high J of the linear fits of the plot of L vs J in the log−log scale. The slope up to 1.27 was obtained for **An-ECz** (Figure S14) This value allows us to presume the contribution of TTA in the EL. The devices based on **An-MCz** did not exhibit slopes higher than 1. Taking into account the detection of long lifetimes and the CT nature of the emission, the possibility of TADF-based EL can be presumed for **An-MCz**. As the T_1 estimated from theoretical calculations has low energy when compared to that of S_1, the possible TADF could occur via RISC from the triplet excited state higher than T_1, possibly approaching the HLCT triplet excited state or via a hot-exciton mechanism (Figure S9). TTA and TADF can also be the competitive processes within the single emitting system. OLEDs based on the EML of **An-tBCz** are characterized by the slopes being close to 1 and higher. The highest obtained slope was 1.79 (Figure S14). The difference in slopes for different devices based on the same emitting species is probably due to the different structures of devices changing the charge balance or the peculiarities of deposition of the layers, stimulating the facilitation of TTA at low J. Anthracene derivatives or anthracene itself can form excimers,[67−70] meaning that the excimer formation could happen (possibly triplet excimer is responsible for the peak at 1.7 eV in the spectrum shown in Figure S9) in some OLEDs in specific conditions, resulting in the enhancement of delayed fluorescence facilitated through TTA. The L−J correlation (Figure S12) is in the accordance with the TrEL signals discussed for **An-tBCz** (Figure 8a), confirming the occurrence of TTA for the compound. We additionally measured the lifetime of the OLED with the EML of the molecular mixture of **An-tBCz** and DPaNIF (Figure S15). The TTA-based devices showed considerably longer operational lifetime than that of the previously reported blue phosphorescent OLED (PhOLED) with FIrpic as the emitter in our lab.[71] The blue PhOLED shows 4 min of LT80 by operating under a luminance of 1000 cd m^{-2}. The TTA-based OLED developed in this work with the EML of the molecular mixture of **An-tBCz** and DPaNIF showed a considerably longer lifetime with LT80 of 38 min operating under the high luminance of 5000 cd m^{-2}.

CONCLUSIONS

Three carbazolyl phenyl anthracenyl benzonitriles with different substituents (*tert*-butyl, methoxy, and methoxyethoxy) attached to the C-3 and C-6 positions of the carbazole moiety were obtained by Stille coupling reactions of bromoanthracene with the corresponding stannanes.

The flat anthracene moiety with extended π-conjugation is responsible for the molecular packing in solid layers of the compounds in a way that stimulates formation of intermolecular interactions favorable for the TTA. Compounds containing ethoxy and methoxyethoxy groups show enhanced thermal stability and photoluminescence quantum yields, arising from delayed fluorescence upon photoexcitation. The *tert*-butyl-containing compound was used for the fabrication of host-free emitting and guest−host emitting layers of the OLEDs. The devices with dopant-free and guest−host emitting layers showed the transient EL signal, which confirmed the delayed emission. Doping-free TTA OLEDs based on TTA showed a maximum external quantum efficiency of 5.9%. The TTA character of the long-living emission was confirmed for the device based on the *tert*-butyl-containing emitter. The plot of brightness vs current density in the log−log scale was found to be 1.79 in the range of current density of 4−12 mA cm^{-2}. The utilization of upconverted triplet excitons in EL resulted in the external quantum efficiency reaching 7.1%. This value is higher than the limit of external quantum efficiency of OLEDs based on prompt fluorescent emitters. The hyperfluorescence assisted by TTA upconversion was achieved utilizing a bicomponent host−guest system without the use of a sensitizer. This study highlights the high potential of blue-emitting donor−acceptor derivatives of anthracene and carbazole exhibiting triplet fusion in OLEDs.

ASSOCIATED CONTENT

Supporting Information

The Supporting Information is available free of charge at https://pubs.acs.org/doi/10.1021/acsaelm.4c00533.

^{1}H NMR and ^{13}C NMR spectra of the compounds; TD-DFT parameters including the triplet state of **An-tBCz**, **An-MCz**, and **An-ECz** in the gas phase; TD-DFT parameters of **An-tBCz**, **An-MCz** and **An-ECz** in toluene solvent; theoretical absorption spectra in gas and solvent phases and experimental spectra in toluene of **An-tBCz**, **An-MCz**, and **An-ECz**; contribution % of different units in FMOs and energy of FMOs with respective E_{gap} of **An-tBCz**, **An-MCz**, and **An-ECz**; DOS plots of the compounds; PL decay curves of the films of **AN-tBCz**, **AN-MCz**, and **AN-ECz** in vacuum at ambient temperature; Jablonski diagram; photo of the films of the compounds deposited by drop casting on the FTO

https://doi.org/10.1021/acsaelm.4c00533
ACS Appl. Electron. Mater. 2024, 6, 4489−4503

substrates made for IP_{PE} determination under UV photoexcitation; PL spectra with different delays applied measured in Argon at liquid nitrogen temperature; lifetimes of the compounds; TOF signals of **An-tBCz**, **An-MCz**, and **An-ECz** recorded for holes and electrons; thicknesses of **An-tBCz**, **An-MCz**, and **An-ECz** recorded by the profilometer Profilm3D; $J-V$ curves, $L-V$ curves, $\eta_{CE}-J$ curves, and $\eta_{PE}-J$ curves of **An-tBCz** OLEDs with various DPaNIF dopant concentrations (6, 9, 12, 18, and 20%); EL characteristics of OLEDs with various DPaNIF dopant concentrations (6, 9, 12, 18, and 20%); EL spectra at 5 and 8 V of **An-tBCz** OLEDs with various DPaNIF dopant concentrations (6, 9, 12, 18, and 20%); plot of dependence of brightness on current density for nonoptimized OLEDs based on EMLs of **An-tBCz**, **An-MCz**, and **An-ECz**; and the lifetime of the OLED with the EML of the molecular mixture of **An-tBCz** and DPaNIF and of the blue PhOLED (PDF)

AUTHOR INFORMATION

Corresponding Authors

Juozas Vidas Grazulevicius − *Department of Polymer Chemistry and Technology, Faculty of Chemical Technology, Kaunas University of Technology, LT-51423 Kaunas, Lithuania;* orcid.org/0000-0002-4408-9727; Email: juozas.grazulevicius@ktu.lt

Pavel Arsenyan − *Latvian Institute of Organic Synthesis, LV-1006 Riga, Latvia;* orcid.org/0000-0001-5875-2799; Email: pavel@osi.lv

Tien-Lung Chiu − *Department of Electrical Engineering, Yuan Ze University, Chungli, Taoyuan 32003, Taiwan;* orcid.org/0000-0002-0631-660X; Email: tlchiu@saturn.yzu.edu.tw

Authors

Oleksandr Bezvikonnyi − *Department of Polymer Chemistry and Technology, Faculty of Chemical Technology, Kaunas University of Technology, LT-51423 Kaunas, Lithuania; Department of Physics, Faculty of Mathematics and Natural Sciences, Kaunas University of Technology, LT-51369 Kaunas, Lithuania*

Audrius Bucinskas − *Department of Polymer Chemistry and Technology, Faculty of Chemical Technology, Kaunas University of Technology, LT-51423 Kaunas, Lithuania*

Alla Petrenko − *Latvian Institute of Organic Synthesis, LV-1006 Riga, Latvia*

Zheng-Yu Wei − *Graduate Institute of Photonics and Optoelectronics and Department of Electrical Engineering, National Taiwan University, Taipei 10617, Taiwan*

Jiun-Haw Lee − *Graduate Institute of Photonics and Optoelectronics and Department of Electrical Engineering, National Taiwan University, Taipei 10617, Taiwan;* orcid.org/0000-0003-3888-0595

Dmytro Volyniuk − *Department of Polymer Chemistry and Technology, Faculty of Chemical Technology, Kaunas University of Technology, LT-51423 Kaunas, Lithuania;* orcid.org/0000-0003-3526-2679

Ehsan Ullah Rashid − *Department of Polymer Chemistry and Technology, Faculty of Chemical Technology, Kaunas University of Technology, LT-51423 Kaunas, Lithuania*

Complete contact information is available at: https://pubs.acs.org/10.1021/acsaelm.4c00533

Notes

The authors declare no competing financial interest.

ACKNOWLEDGMENTS

This work was supported by the Project of Scientific Cooperation Program between Latvia, Lithuania, and Taiwan (grant LV-LT-TW/2023) and Research Council of Lithuania (LMTLT), Agreement no. S-LLT-22-4. This project has also received funding from the Research Council of Lithuania (LMTLT), agreement no. S-MIP-22-78. The study has also received funding and support from the National Science and Technology Council (NSTC), Taiwan, under grants NSTC 111-2923-E-155-002-MY3.

REFERENCES

(1) Tankelevičiūtė, E.; Samuel, I. D. W.; Zysman-Colman, E. The Blue Problem: OLED Stability and Degradation Mechanisms. *J. Phys. Chem. Lett.* **2024**, *15* (4), 1034−1047.

(2) Kandasamy, N.; Keerthi, N.; Jeyasekaran, J. Mixed Ligand Copper(I) Complexes as Emitters Enable Higher OLED Device Performance for Energy-Harvesting Applications. *ACS Appl. Electron. Mater.* **2023**, *5* (9), 4805−4815.

(3) Jouaiti, A.; Huang, D. C.; Giuso, V.; Cebrián, C.; Mercandelli, P.; Wang, K. H.; Chang, C. H.; Mauro, M. True- to Sky-Blue Emitters Bearing the Thiazolo[5,4- d]Thiazole Electron Acceptor for Single and Tandem Organic Light-Emitting Diodes. *ACS Appl. Electron. Mater.* **2023**, *5* (5), 2781−2792.

(4) Li, D.; Guo, B.; Shen, Y.; Li, J.; Huang, Y. Making Image More Energy Efficient for OLED Smart Devices. *Mob. Inf. Syst.* **2016**, *2016*, 6575931.

(5) Siddiqui, I.; Kumar, S.; Tsai, Y. F.; Gautam, P.; Shahnawaz; Kesavan, K.; Lin, J. T.; Khai, L.; Chou, K. H.; Choudhury, A.; Grigalevicius, S.; Jou, J. H. Status and Challenges of Blue OLEDs: A Review. *Nanomaterials* **2023**, *13*, 2521.

(6) Jang, K.; O'brien, B. Advanced Displays, Materials Market Trends, and Unsettled Challenges. *Inf. Dispersion* **2023**, *39* (6), 31−34.

(7) Mikhnenko, O. V.; Blom, P. W. M.; Nguyen, T. Q. Exciton Diffusion in Organic Semiconductors. *Energy Environ. Sci.* **2015**, *8*, 1867−1888.

(8) Dias, F. B.; Penfold, T. J.; Monkman, A. P. Photophysics of Thermally Activated Delayed Fluorescence Molecules. *Methods Appl. Fluoresc.* **2017**, *5*, 012001.

(9) Klimash, A.; Prlj, A.; Yufit, D. S.; Mallick, A.; Curchod, B. F. E.; McGonigal, P. R.; Skabara, P. J.; Etherington, M. K. From Phosphorescence to Delayed Fluorescence in One Step: Tuning Photophysical Properties by Quaternisation of an Sp2-Hybridised Nitrogen Atom. *J. Mater. Chem. C* **2022**, *10* (25), 9484−9491.

(10) Li, Q.; He, Y.; Lv, K.; Ma, H. Theoretical Study on the Origin of the Dual Phosphorescence Emission from Organic Aggregates at Room Temperature. *Spectrochim Acta A Mol Biomol Spectrosc.* **2023**, *287*, 122077.

(11) Dong, X.; Li, R.; Zheng, Y.; Huo, J.; Cao, Y.; Shi, H. Synthesis, Photoluminescence and Electroluminescence Properties of a New Blue Emitter with Aggregation-Induced Emission and Thermally Activated Delayed Fluorescence Characteristics. *Spectrochim Acta A Mol Biomol Spectrosc.* **2023**, *291*, 122344.

(12) Zhu, Y.; Kong, L.; Yang, J. X. Multifunctional Behavior of a Carbazole Derivative: Red Phosphorescent Emission, Aggregation-Induced Long-Life Exciton and Light-Emitting Diode Application. *Spectrochim Acta A Mol Biomol Spectrosc.* **2023**, *290*, 122208.

(13) Lee, J. H.; Chen, C. H.; Lee, P. H.; Lin, H. Y.; Leung, M. K.; Chiu, T. L.; Lin, C. F. Blue Organic Light-Emitting Diodes: Current Status, Challenges, and Future Outlook. *J. Mater. Chem. C* **2019**, *7*, 5874−5888.

(14) Giebink, N. C.; D'Andrade, B. W.; Weaver, M. S.; MacKenzie, P. B.; Brown, J. J.; Thompson, M. E.; Forrest, S. R. Intrinsic

Luminance Loss in Phosphorescent Small-Molecule Organic Light Emitting Devices Due to Bimolecular Annihilation Reactions. *J. Appl. Phys.* **2008**, *103* (4), 44509.
(15) Lee, J.; Jeong, C.; Batagoda, T.; Coburn, C.; Thompson, M. E.; Forrest, S. R. Hot Excited State Management for Long-Lived Blue Phosphorescent Organic Light-Emitting Diodes. *Nat. Commun.* **2017**, *8*, 15566.
(16) Kim, E.; Park, J.; Jun, M.; Shin, H.; Baek, J.; Kim, T.; Kim, S.; Lee, J.; Ahn, H.; Sun, J.; Ko, S. B.; Hwang, S. H.; Lee, J. Y.; Chu, C.; Kim, S. Highly Efficient and Stable Deep-Blue Organic Light-Emitting Diode Using Phosphor-Sensitized Thermally Activated Delayed Fluorescence. *Sci. Adv.* **2022**, *8* (41), No. eabq1641.
(17) Zhao, H.; Kim, J.; Ding, K.; Jung, M.; Li, Y.; Ade, H.; Lee, J. Y.; Forrest, S. R. Control of Host-Matrix Morphology Enables Efficient Deep-Blue Organic Light-Emitting Devices. *Adv. Mater.* **2023**, *35* (12), 2210794.
(18) Chiang, C. J.; Kimyonok, A.; Etherington, M. K.; Griffiths, G. C.; Jankus, V.; Turksoy, F.; Monkman, A. P. Ultrahigh Efficiency Fluorescent Single and Bi-Layer Organic Light Emitting Diodes: The Key Role of Triplet Fusion. *Adv. Funct. Mater.* **2013**, *23* (6), 739−746.
(19) Stockert, J. C.; Blazquez-Castro, A. Non-Linear Optics. *Fluorescence Microscopy in Life Sciences*; Bentham Science Publishers, 2017; pp 642−686..
(20) Dzebo, D.; Börjesson, K.; Gray, V.; Moth-Poulsen, K.; Albinsson, B. Intramolecular Triplet-Triplet Annihilation Upconversion in 9,10-Diphenylanthracene Oligomers and Dendrimers. *J. Phys. Chem. C* **2016**, *120* (41), 23397−23406.
(21) Van der Zee, B.; Li, Y.; Wetzelaer, G. J. A. H.; Blom, P. W. M. Efficiency of Polymer Light-Emitting Diodes: A Perspective. *Adv. Mater.* **2022**, *34*, 2100249.
(22) Bennison, M. J.; Collins, A. R.; Zhang, B.; Evans, R. C. Organic Polymer Hosts for Triplet-Triplet Annihilation Upconversion Systems. *Macromolecules* **2021**, *54*, 5287−5303.
(23) Franca, L. G.; Dos Santos, P. L.; Pander, P.; Cabral, M. G. B.; Cristiano, R.; Cazati, T.; Monkman, A. P.; Bock, H.; Eccher, J. Delayed Fluorescence by Triplet-Triplet Annihilation from Columnar Liquid Crystal Films. *ACS Appl. Electron. Mater.* **2022**, *4* (7), 3486−3494.
(24) Bohne, C.; Abuin, E. B.; Scaiano, J. C. Characterization of the Triplet-Triplet Annihilation Process of Pyrene and Several Derivatives under Laser Excitation. *J. Am. Chem. Soc.* **1990**, *112* (11), 4226−4231.
(25) Sakamoto, Y.; Tamai, Y.; Ohkita, H. Sensitizer-Host-Annihilator Ternary-Cascaded Triplet Energy Landscape for Efficient Photon Upconversion in the Solid State. *J. Chem. Phys.* **2020**, *153* (16), 161102.
(26) Xing, L.; Zhu, Z. L.; He, J.; Qiu, Z.; Yang, Z.; Lin, D.; Chen, W. C.; Yang, Q.; Ji, S.; Huo, Y.; Lee, C. S. Anthracene-Based Fluorescent Emitters toward Superior-Efficiency Nondoped TTA-OLEDs with Deep Blue Emission and Low Efficiency Roll-Off. *Chem. Eng. J.* **2021**, *421*, 127748.
(27) Wang, R.; Hu, D.; Xing, L.; Lu, Z.; Zhu, Y.; Mao, Z.; Chen, W. cheng; Huo, Y.; Ji, S. Anthracene Derivatives with Hot Exciton and TTA Process for High-Efficiency Organic Light-Emitting Diodes. *Dyes Pigm.* **2023**, *215*, 111276.
(28) Nalaoh, P.; Sungworawongpana, N.; Chasing, P.; Waengdongbung, W.; Funchien, P.; Kaiyasuan, C.; Sudyoadsuk, T.; Promarak, V. A Dimeric π-Stacking of Anthracene Inducing Efficiency Enhancement in Solid-State Fluorescence and Non-Doped Deep-Blue Triplet-Triplet Annihilation Organic Light-Emitting Diodes. *Adv. Opt. Mater.* **2021**, *9* (17), 2100500.
(29) Li, W.; Chasing, P.; Nalaoh, P.; Chawanpunyawat, T.; Chantanop, N.; Sukpattanacharoen, C.; Kungwan, N.; Wongkaew, P.; Sudyoadsuk, T.; Promarak, V. Deep-Blue High-Efficiency Triplet-Triplet Annihilation Organic Light-Emitting Diodes Using Hydroxyl-Substituted Tetraphenylimidazole-Functionalized Anthracene Fluorescent Emitters. *J. Mater. Chem. C* **2022**, *10* (27), 9968−9979.
(30) Cao, C.; Yang, G. X.; Tan, J. H.; Shen, D.; Chen, W. C.; Chen, J. X.; Liang, J. L.; Zhu, Z. L.; Liu, S. H.; Tong, Q. X.; Lee, C. S. Deep-Blue High-Efficiency Triplet-Triplet Annihilation Organic Light-Emitting Diodes Using Donor- and Acceptor-Modified Anthracene Fluorescent Emitters. *Mater. Today Energy* **2021**, *21*, 100727.
(31) Wang, Z.; Yang, T.; Dong, S.; Wen, Z.; Xu, H.; Miao, Y.; Wang, H.; Yu, J. Anthracene and Carbazole Based Asymmetric Fluorescent Materials for High-Efficiency Deep-Blue Non-Doped Organic Light Emitting Devices with CIEy = 0.06. *Dyes Pigm.* **2022**, *199*, 110047.
(32) Ledwon, P. Recent Advances of Donor-Acceptor Type Carbazole-Based Molecules for Light Emitting Applications. *Org. Electron.* **2019**, *75*, 105422.
(33) Behera, S. K.; Costa, R. D. Emerging Hyperfluorescent Emitters for Solid-State Lighting. *J. Mater. Chem. C* **2023**, *11* (40), 13647−13656.
(34) Deori, U.; Yadav, N.; Nanda, G. P.; Kumawat, K. L.; Rajamalli, P. Systematic Study to Choose Appropriate Materials Combination for Green Hyperfluorescent Organic Light-Emitting Diodes. *ACS Appl. Electron. Mater.* **2023**, *5* (9), 4959−4967.
(35) Gawale, Y.; Ansari, R.; Naveen, K. R.; Kwon, J. H. Forthcoming Hyperfluorescence Display Technology: Relevant Factors to Achieve High-Performance Stable Organic Light Emitting Diodes. *Front. Chem.* **2023**, *11*, 1211345.
(36) Stavrou, K.; Madayanad Suresh, S.; Hall, D.; Danos, A.; Kukhta, N. A.; Slawin, A. M. Z.; Warriner, S.; Beljonne, D.; Olivier, Y.; Monkman, A.; Zysman-Colman, E. Emission and Absorption Tuning in TADF B,N-Doped Heptacenes: Toward Ideal-Blue Hyperfluorescent OLEDs. *Adv. Opt. Mater.* **2022**, *10* (17), 2200688.
(37) Chan, C. Y.; Tanaka, M.; Lee, Y. T.; Wong, Y. W.; Nakanotani, H.; Hatakeyama, T.; Adachi, C. Stable Pure-Blue Hyperfluorescence Organic Light-Emitting Diodes with High-Efficiency and Narrow Emission. *Nat. Photonics* **2021**, *15*, 203−207.
(38) Chan, C. Y.; Tanaka, M.; Lee, Y. T.; Wong, Y. W.; Nakanotani, H.; Hatakeyama, T.; Adachi, C. Author Correction: Stable pure-blue hyperfluorescence organic light-emitting diodes with high-efficiency and narrow emission. *Nat. Photonics* **2021**, *15*, 245.
(39) Zhang, L.; Ding, L.; Zhou, S.; Zhang, F.; Gu, P. An Unexpected Fluorescent Emission of Anthracene Derivatives in the Solid State. *Dyes Pigm.* **2023**, *210*, 110991.
(40) Qin, W.; Yang, Z.; Jiang, Y.; Lam, J. W. Y.; Liang, G.; Kwok, H. S.; Tang, B. Z. Construction of Efficient Deep Blue Aggregation-Induced Emission Luminogen from Triphenylethene for Nondoped Organic Light-Emitting Diodes. *Chem. Mater.* **2015**, *27* (11), 3892−3901.
(41) Wex, B.; Kaafarani, B. R. Perspective on Carbazole-Based Organic Compounds as Emitters and Hosts in TADF Applications. *J. Mater. Chem. C* **2017**, *5* (34), 8622−8653.
(42) Li, C.; Duan, C.; Han, C.; Xu, H. Secondary Acceptor Optimization for Full-Exciton Radiation: Toward Sky-Blue Thermally Activated Delayed Fluorescence Diodes with External Quantum Efficiency of ≈30%. *Adv. Mater.* **2018**, *30* (50), 1804228.
(43) Frisch, M. J.; Trucks, G. W.; Schlegel, H. B.; Scuseria, G. E.; Robb, M. A.; Cheeseman, J. R.; Scalmani, G.; Barone, V.; Petersson, G. A.; Nakatsuji, H.; Li, X.; Caricato, M.; Marenich, A. V.; Bloino, J.; Janesko, B. G.; Gomperts, R.; Mennucci, B.; Hratch, J. B. *Gaussian 16*, 2016.
(44) Lutnæs, O. B.; Ruden, T. A.; Helgaker, T. The Performance of Hybrid Density Functional Theory for the Calculation of Indirect Nuclear Spin-Spin Coupling Constants in Substituted Hydrocarbons. *Magn. Reson. Chem.* **2004**, *42* (S1), S117−S127.
(45) He, X.; Ren, S.; Liu, H.; Zhao, S.; Liu, F.; Du, C.; Min, J.; Zhang, H.; Lu, P. Efficient Nondoped Pure Blue Organic Light-Emitting Diodes Based on an Anthracene and 9,9-Diphenyl-9,10-Dihydroacridine Derivative. *Chem.—Asian J.* **2020**, *15* (1), 163−168.
(46) Arsenyan, P.; Ikaunieks, M.; Belyakov, S. Stille Coupling Approaches for the Synthesis of 8-Aryl Guanines. *Tetrahedron Lett.* **2007**, *48* (6), 961−964.
(47) D'Andrade, B. W.; Datta, S.; Forrest, S. R.; Djurovich, P.; Polikarpov, E.; Thompson, M. E. Relationship between the Ionization and Oxidation Potentials of Molecular Organic Semiconductors. *Org. Electron.* **2005**, *6* (1), 11−20.

https://doi.org/10.1021/acsaelm.4c00533
ACS Appl. Electron. Mater. 2024, 6, 4489−4503

(48) Quezada-Borja, J. D.; Rodríguez-Valdez, L. M.; Palomares-Báez, J. P.; Chávez-Rojo, M. A.; Landeros-Martinez, L. L.; Martínez-Ceniceros, M. C.; Rojas-George, G.; García-Montoya, I. A.; Sánchez-Bojorge, N. A. Design of New Hole Transport Materials Based on Triphenylamine Derivatives Using Different π-Linkers for the Application in Perovskite Solar Cells. A Theoretical Study. *Front. Chem.* **2022**, *10*, 907556.
(49) Rashid, E. U.; Hadia, N. M. A.; Iqbal, J.; Mehmood, R. F.; Somaily, H. H.; Akram, S. J.; Shawky, A. M.; Khan, M. I.; Noor, S.; Khera, R. A. Engineering of W-Shaped Benzodithiophenedione-Based Small Molecular Acceptors with Improved Optoelectronic Properties for High Efficiency Organic Solar Cells. *RSC Adv.* **2022**, *12* (34), 21801−21820.
(50) Pitaro, M.; Alonso, J. S.; Di Mario, L.; Garcia Romero, D.; Tran, K.; Zaharia, T.; Johansson, M. B.; Johansson, E. M. J.; Loi, M. A. A Carbazole-Based Self-Assembled Monolayer as the Hole Transport Layer for Efficient and Stable Cs0.25FA0.75Sn0.5Pb0.5I3 Solar Cells. *J. Mater. Chem. A* **2023**, *11* (22), 11755−11766.
(51) Pitaro, M.; Alonso, J. E. S.; Di Mario, L.; Romero, D. G.; Tran, K.; Kardula, J.; Zaharia, T.; Johansson, M. B.; Johansson, E. M. J.; Chiechi, R. C.; Loi, M. A. Tuning the Surface Energy of Hole Transport Layers Based on Carbazole Self-Assembled Monolayers for Highly Efficient Sn/Pb Perovskite Solar Cells. *Adv. Funct. Mater.* **2023**, 2306571.
(52) Coropceanu, V.; Cornil, J.; da Silva Filho, D. A.; Olivier, Y.; Silbey, R.; Brédas, J. L. Charge Transport in Organic Semiconductors. *Chem. Rev.* **2007**, *107*, 926−952.
(53) Hutchison, G. R.; Ratner, M. A.; Marks, T. J. Hopping Transport in Conductive Heterocyclic Oligomers: Reorganization Energies and Substituent Effects. *J. Am. Chem. Soc.* **2005**, *127* (7), 2339−2350.
(54) Malagoli, M.; Coropceanu, V.; Da Silva Filho, D. A.; Brédas, J. L. A Multimode Analysis of the Gas-Phase Photoelectron Spectra in Oligoacenes. *J. Chem. Phys.* **2004**, *120* (16), 7490−7496.
(55) Rashid, E. U.; Hadia, N. M. A.; Shawky, A. M.; Ijaz, N.; Essid, M.; Iqbal, J.; Alatawi, N. S.; Ans, M.; Khera, R. A. Quantum Modeling of Dimethoxyl-Indaceno Dithiophene Based Acceptors for the Development of Semiconducting Acceptors with Outstanding Photovoltaic Potential. *RSC Adv.* **2023**, *13* (7), 4641−4655.
(56) Rashid, E. U.; Hadia, N. M. A.; Alaysuy, O.; Iqbal, J.; Hessien, M. M.; Mersal, G. A. M.; Mehmood, R. F.; Shawky, A. M.; Khan, M. I.; Khera, R. A. Quantum Chemical Modification of Indaceno Dithiophene-Based Small Acceptor Molecules with Enhanced Photovoltaic Aspects for Highly Efficient Organic Solar Cells. *RSC Adv.* **2022**, *12* (44), 28608−28622.
(57) Fonseca Guerra, C.; Handgraaf, J. W.; Baerends, E. J.; Bickelhaupt, F. M. Voronoi Deformation Density (VDD) Charges: Assessment of the Mulliken, Bader, Hirshfeld, Weinhold, and VDD Methods for Charge Analysis. *J. Comput. Chem.* **2004**, *25* (2), 189−210.
(58) Bujaldón, R.; Vilche, A.; Puigdollers, J.; Puigjaner, C.; Alcobé, X.; Velasco, D. Insight into the Diindolo[3,2-b:2′,3′-h]Carbazole Core as an Air-Stable Semiconductor for OTFTs. *ACS Appl. Electron. Mater.* **2023**, *5* (7), 3675−3684.
(59) Roszak, K.; Maciejewski, A.; Katrusiak, A.; Krystkowiak, E. Solute - Solvent Repulsion Effects on the Absorption Spectra of Anthracene in N-Hexane Investigated under High Pressure. *Spectrochim Acta A Mol Biomol Spectrosc.* **2023**, *299*, 122822.
(60) Hagberg, D. P.; Yum, J. H.; Lee, H. J.; De Angelis, F.; Marinado, T.; Karlsson, K. M.; Humphry-Baker, R.; Sun, L.; Hagfeldt, A.; Grätzel, M.; Nazeeruddin, M. K. Molecular Engineering of Organic Sensitizers for Dye-Sensitized Solar Cell Applications. *J. Am. Chem. Soc.* **2008**, *130* (19), 6259−6266.
(61) Cesaretti, A.; Cai, Z.; Kim, J.; Kim, H.; Lei, Y.; Carlotti, B. Dual-State Emission and Two-Photon Absorption Tuned by Benzonitrile Substitution in 2,3,4,5-Tetraphenyl-1H-Pyrrole. *ChemPhotoChem* **2023**, *7* (6), No. e202300040.
(62) Serevičius, T.; Skaisgiris, R.; Kreiza, G.; Dodonova, J.; Kazlauskas, K.; Orentas, E.; Tumkevičius, S.; Juršėnas, S. TADF Parameters in the Solid State: An Easy Way to Draw Wrong Conclusions. *J. Phys. Chem. A* **2021**, *125* (7), 1637−1641.
(63) Funahashi, M. Time-of-Flight Method for Determining the Drift Mobility in Organic Semiconductors. *Organic Semiconductors for Optoelectronics*; John Wiley & Sons, 2021; pp 161−178..
(64) Gudeika, D.; Miasojedovas, A.; Bezvikonnyi, O.; Volyniuk, D.; Gruodis, A.; Jursenas, S.; Grazulevicius, J. V. Differently Substituted Benzothiadiazoles as Charge-Transporting Emitters for Fluorescent Organic Light-Emitting Diodes. *Dyes Pigm.* **2019**, *166*, 217−225.
(65) Qiao, X.; Yuan, P.; Ma, D.; Ahamad, T.; Alshehri, S. M. Electrical Pumped Energy Up-Conversion: A Non-Linear Electroluminescence Process Mediated by Triplet-Triplet Annihilation. *Org. Electron.* **2017**, *46*, 1−6.
(66) Shukla, A.; Hasan, M.; Banappanavar, G.; Ahmad, V.; Sobus, J.; Moore, E. G.; Kabra, D.; Lo, S. C.; Namdas, E. B. Controlling Triplet-Triplet Upconversion and Singlet-Triplet Annihilation in Organic Light-Emitting Diodes for Injection Lasing. *Commun. Mater.* **2022**, *3* (1), 27.
(67) Zhao, C.; Cai, X.; Ma, Z.; Shi, J.; Xu, L.; Wang, H. Excimer Formation from Particially Overlapped Anthracene Dimer Based on Saddle-Shaped Cyclooctatetrathiophene as Spacer. *J. Photochem. Photobiol., A* **2018**, *355*, 318−325.
(68) Arnold, S.; Hassan, N. Triplet Exciton Lifetime under Pressure in "Pure Anthracene. *J. Chem. Phys.* **1983**, *78* (9), 5606−5611.
(69) Schillmöller, T.; Herbst-Irmer, R.; Stalke, D. Insights into Excimer Formation Factors from Detailed Structural and Photophysical Studies in the Solid-State. *Adv. Opt. Mater.* **2021**, *9* (8), 2001814.
(70) Liu, H.; Yao, L.; Li, B.; Chen, X.; Gao, Y.; Zhang, S.; Li, W.; Lu, P.; Yang, B.; Ma, Y. Excimer-Induced High-Efficiency Fluorescence Due to Pairwise Anthracene Stacking in a Crystal with Long Lifetime. *Chem. Commun.* **2016**, *52* (46), 7356−7359.
(71) Chiu, T. L.; Chen, H. J.; Hsieh, Y. H.; Huang, J. J.; Leung, M. kit. High-Efficiency Blue Phosphorescence Organic Light-Emitting Diode with Ambipolar Carbazole-Triazole Host. *J. Phys. Chem. C* **2015**, *119* (29), 16846−16852.

https://doi.org/10.1021/acsaelm.4c00533
ACS Appl. Electron. Mater. 2024, 6, 4489−4503